

Destriping of Multispectral Remote Sensing Image Using Low-Rank Tensor Decomposition

Yong Chen , Ting-Zhu Huang , and Xi-Le Zhao 

Abstract—Multispectral image (MSI) destriping is a challenging topic and has been attracting much research attention in remote sensing area due to its importance in improving the image qualities and subsequent applications. The existing destriping methods mainly focus on matrix-based modeling representation, which fails to fully discover the correlation of the stripe component in both spatial dimensions. In this paper, we propose a novel low-rank tensor decomposition framework based MSI destriping method by decomposing the striped image into the image component and stripe component. Specifically, for the image component, we use the anisotropic spatial unidirectional total variation (TV) and spectral TV regularization to enhance the piecewise smoothness in both spatial and spectral domains. Moreover, for the stripe component, we adopt tensor Tucker decomposition and $\ell_{2,1}$ -norm regularization to model the spatial correlation and group sparsity characteristic among all bands, respectively. An efficient algorithm using the augmented Lagrange multiplier method is designed to solve the proposed optimization model. Experiments under various cases of simulated data and real-world data demonstrate the effectiveness of the proposed model over the existing single-band and MSI destriping methods in terms of the qualitative and quantitative.

Index Terms—Augmented Lagrange multiplier (ALM), destriping, low-rank tensor decomposition (LRTD), multispectral image (MSI), Tucker decomposition.

I. INTRODUCTION

WITH the development of remote sensing technologies, a multispectral image (MSI) normally consists of dozens or even hundreds of spectral band images in remote sensing. Due to the wealth spatial and spectral information of MSI in the real scene, MSI has attracted attention and is very useful for many practical applications, such as environmental monitoring, urban planning, and military surveillance. However, multispectral imaging sensor inevitably generates some stripe noises into the collected MSI data during the imaging process. There are mainly two different types of remote sensing imaging system push-broom and cross-track imaging devices that are contam-

Manuscript received July 27, 2018; revised September 23, 2018; accepted October 19, 2018. Date of publication November 12, 2018; date of current version December 31, 2018. This work was supported in part by the National Natural Science Foundation of China under Grant 61772003, Grant 61876203 and Grant 61702083, and in part by the Fundamental Research Funds for the Central Universities under Grant ZYGX2016J132. (Corresponding author: Ting-Zhu Huang.)

The authors are with the School of Mathematical Sciences/Resarch Center for Image and Vision Computing, University of Electronic Science and Technology of China, Chengdu 611731, China (e-mail: chenyong1872008@163.com; tingzhuhuang@126.com; xlzhao122003@163.com).

Color versions of one or more of the figures in this paper are available online at <http://ieeexplore.ieee.org>.

Digital Object Identifier 10.1109/JSTARS.2018.2877722

inated with stripes. The main reasons for creating stripes are the inconsistent response among different sensors and calibration error [1]. The stripe noise in MSI seriously influences the visual quality of the imagery and poses great challenges for subsequent processing, including unmixing [2], image fusion [3], target detection [4], and classification [5]. Especially, the authors in [5] used the destriped technique to enhance the image classification for forest encroachment mapping. Therefore, to obtain better visual quality and improve the ability of the subsequent application of the MSI, it is an important preprocessing step to remove the stripe noise (destriping) in MSI.

To date, numerous destriping methods have been proposed for restoring the remote sensing image. They can be split into two categories: single-band remote sensing image destriping methods and destriping methods based on MSI or hyperspectral image (HSI). The goal of this paper addresses the MSI stripe noise removal. Compared with single-image destriping, the application of MSI destriping is more useful, because it can preserve the abundant spectral information in the restored remote sensing image.

For the single-band remote sensing image destriping issue, existing methods can be roughly separated into three categories: filtering-based methods, statistics-based methods, and optimization-model-based methods. Filtering-based methods, e.g., Fourier domain filter [1], [6], wavelet analysis [7], [8], and the Fourier-wavelet combined domain filter [9], [10], are the straightforward ideas for image destriping. These methods depend on the hypothesis that the stripe component is the periodic distribution in the image and can be isolated in the power spectrum [1]. However, some useful signals with the same frequency may be filtered out along with the stripes, which results in obviously blurring and ringing artifacts in the restored image [1], [8]. Statistic-based methods are also usually used for single-image destriping due to the fact that these methods are easy to perform, such as moment matching [11], [12] and histogram matching [13]–[15]. These approaches concentrate on the statistical property of digital numbers for each sensor. However, they are greatly determined by the pre-established reference moment or histogram.

In recent, optimization-based methods have attracted much attention and are extensively used for stripe noise removal. The main idea of these methods is that they treat the destriping problem as an ill-posed inverse issue and construct an optimization model by incorporating some regularization terms. Shen and Zhang [16] first proposed a maximum *a posteriori* framework and incorporated Huber–Markov model as the prior for remote

sensing image destriping and inpainting. In [17], the authors successively proposed a sophisticated unidirectional total variational (UTV) model for MODIS data destriping by excavating the directional characteristic of stripes. Thereupon, to improve the destriping performance of UTV model, many researchers have proposed some modified UTV model by incorporating other regularization terms [18]–[21]. In [18], the authors proposed a joint model combining UTV model and framelet regularization to simultaneously remove random noise and stripe noise. In [21], Liu *et al.* used the one-dimensional (1-D) statistical property to guide and add to the UTV model for stripe noise removal. Moreover, there is a different processing angle to remove stripe noise by estimating and separating the stripe component from the striped image [22]–[25]. In [24], the authors achieved the destriping by separating the stripe component based on a full analysis of the various stripe properties. In our recent work [22], we introduced the group sparsity prior to remove stripes as well as precisely extracting the stripe component. In [26] and [27], the authors treated the image and stripe components equally and converted the image destriping task as an image decomposition problem, which can simultaneously integrate the prior knowledge of the image component and stripe component.

The above-mentioned methods mainly focus on single-band image destriping, which fail to take full advantage of the spectral information in MSI and HSI. To track this issue, many MSI and HSI destriping methods have been proposed to improve the restoration performance for remote sensing image. Regarding the stripe noise as the sparse noise, some HSI restoration methods have been developed to remove the stripe noise [28]–[30]. By using the high spectral correlation between the image in different bands and considering the local manifold structure of the hyperspectral data space, Lu *et al.* [31] proposed a graph-regularized low-rank representation (LRR) model for destriping of HSI. In [32], the authors proposed an anisotropic spectral-spatial total variation (TV) model for multispectral remote sensing image destriping, which can promote the smoothness of the image in the spatial and spectral domain. Based on the low-rank-based single-image decomposition model [26], the authors extended this model to MSI destriping by incorporating the spectral information. To improve the destriping performance of [26] in dense stripes with the high-intensity case, the low-rank and nonlocal TV model was proposed in [33]. Cerra *et al.* [34] proposed an unmixing-based method for HSI destriping and inpainting.

Although the above of these destriping methods have obtained a satisfactory destriping performance for multispectral remote sensing image, they still neglect some important priors for the destriping of MSI or HSI. The method in [32] only considered the priors of the image component in the spatial-spectral dimension, whereas it fails to take into account the priors for the stripe component. In [26] and [33], the authors used the band-by-band matrix low rank prior to describe the structural characteristic for the stripe component, but they cannot take the advantage of the high correlation among the stripe component in different bands. Thus, how to make full use of this high correlation to improve the destriping performance is a noteworthy problem. Moreover,

most of the destriping methods model and characterize the image component and stripe component under a matrix framework. In fact, the MSI or HSI can be viewed as a high-order tensor data. From tensor perspective, the tensor decomposition of the striped image and the high correlation of the stripe component are shown in Fig. 1. As shown in Fig. 1(b-1) and (c-1), we can clearly see that both the spatial mode unfolding images of the stripe component have a more intuitive structure compared with the image component. To qualitatively characterize these fine structures, we present the curves of the normalized singular values of the two unfolding matrices for the image component and stripe component, which are shown in Fig. 1(b-2) and (b-3), and (c-2) and (c-3), respectively. From the figure to see, we can clearly see that the drastically decaying trend of Fig. 1(c-2) and (c-3) is more faster than Fig. 1(b-2) and (b-3), which indicates that the strong spatial correlation of the stripe component is more significant than the image component in different bands.

Motivated by the high correlation of the stripe component in different bands, in this work, we propose a low-rank tensor decomposition (LRTD) model for the task of MSI destriping. Since the tensor Tucker decomposition approach can effectively depict the high correlation of the tensor data [28], [35], [36], we design it to characterize the high correlation of the stripe component in both spatial dimensions. Compared to the previous band-by-band matrix LRR for the stripe component, low-rank Tucker decomposition can simultaneously encode the high correlation of the stripe component in both spatial correlations. Moreover, the stripe component also presents the group sparsity prior in each band shown in Fig. 1(a-3), and we design $\ell_{2,1}$ norm to track it. To preserve the local piecewise smoothness of the image component in both spatial horizontal and spectral directions, we adopt anisotropic spatial unidirectional TV and spectral TV to regularize the image component. Detailed modeling of our work can be found in Section III-B. To efficiently solve the proposed model, an augmented Lagrange multiplier (ALM) method is designed to optimize the proposed model. The experiments on simulated data with different stripe cases and real data demonstrate that our proposed method achieves better destriping performance than the existing single-band and MSI destriping approaches. The main contributions of this paper are summarized as follows.

- 1) To the best of our knowledge, we are the first to model the MSI destriping task in a LRTD framework. Compared to the matrix-based image representation, this tensor-based representation well preserves the high correlation of the image in different bands.

- 2) The low-rank Tucker decomposition is introduced to depict the high correlation of the stripe component in both spatial modes, which can precisely isolate the stripe component from the striped image.

- 3) We design an efficient ALM method to solve the proposed LRTD model and perform superior destriping performance over the existing single-band and MSI destriping methods on various stripe degradation cases, especially when the stripe component is very dense and is of high intensity in the image.

The remainder of this paper is organized as follows. In Section II, we give some notations and preliminaries for the

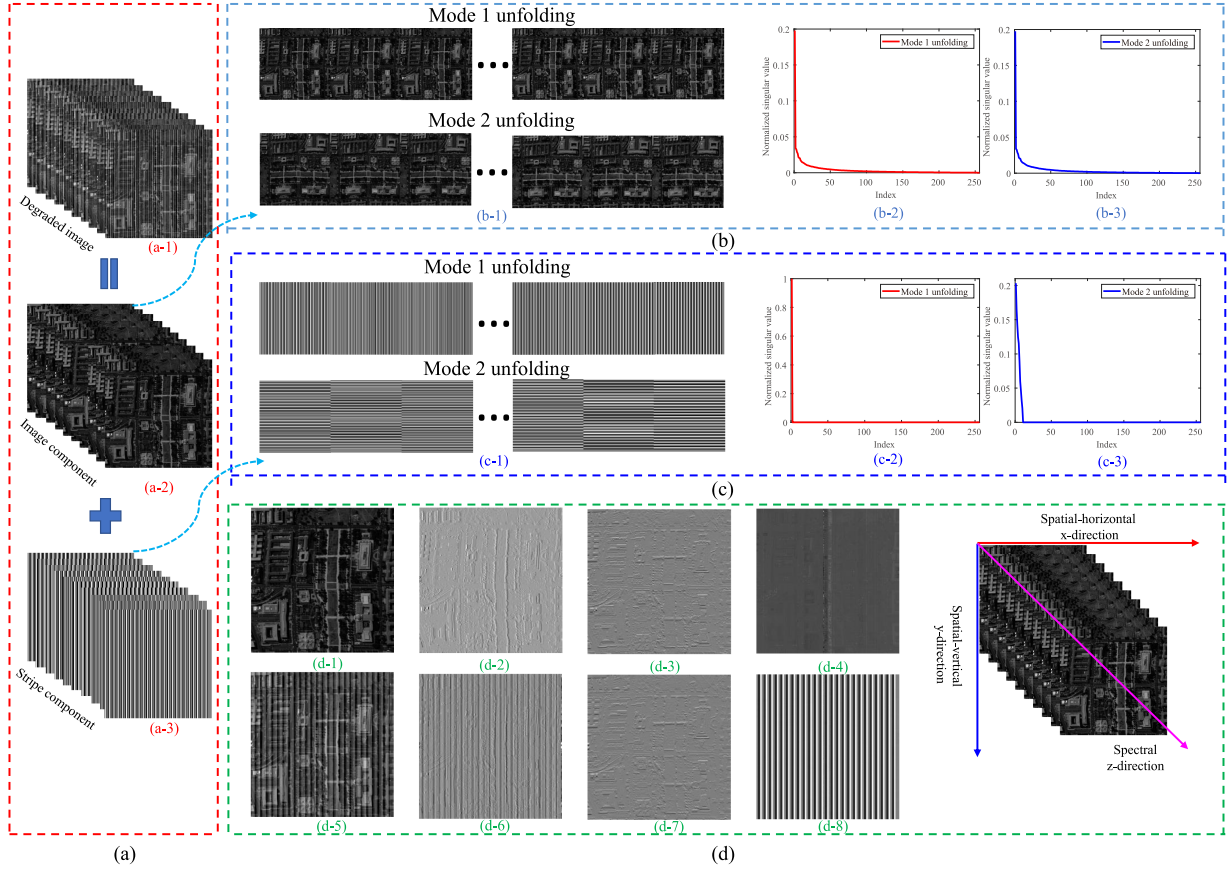


Fig. 1. Illustration of the image component and stripe component priors. (a) LRTD framework. (a-1) Degraded image, (a-2) image component, (a-3) stripe component. (b-1) Mode 1 and mode 2 unfoldings of the image component (a-2), (b-2,3) distribution of normalized singular values in mode 1 and mode 2 unfoldings of the image component. (c-1) Mode 1 and mode 2 unfoldings of the stripe component (a-3), (c-2,3) distribution of normalized singular values in mode 1 and mode 2 unfoldings of the stripe component. (d) Derivation characteristics of the image component and degraded image. (d-1) Band 4 of (a-2), (d-2,3,4) the spatial horizontal, spatial vertical, and spectral derivation images of (d-1), respectively. (d-5) Band 4 of (a-1), (d-6,7,8) the spatial horizontal, spatial vertical, and spectral derivation images of (d-5), respectively.

tensor. The detailed formulation of our LRTD model and the ALM solver are presented in Section III. In Section IV, we present extensive experimental results on both simulated and real data to demonstrate the effectiveness of our method, and we then give the discussion of the proposed model. Finally, we conclude this paper in Section V.

II. NOTATIONS AND PRELIMINARIES

A tensor can be regarded as a multi-index numerical array, and the number of its modes or dimensions represent its order. In this section, we first introduce some tensor related notions and preliminaries as follows. Following [37], in this paper, we use capitalized calligraphic letters for tensors (high-order data), e.g., \mathcal{X} . Matrices (second-order data) are represented as capitalized boldface letters, e.g., \mathbf{X} . A vector (first-order data) is denoted as boldface lowercase letters, e.g., \mathbf{x} , and we denote scalars as lowercase letters, e.g., x . An N -mode tensor is defined as $\mathcal{X} \in \mathbb{R}^{I_1 \times I_2 \times \dots \times I_N}$, and we denote its (i_1, i_2, \dots, i_N) element as x_{i_1, i_2, \dots, i_N} .

Fibers are the higher-order analogue of matrix rows and columns. A fiber is defined by fixing every index, but one. Third-order tensors have column, row, and tube fibers, denoted

by $\mathbf{x}_{:jk}$, $\mathbf{x}_{ik:}$, and $\mathbf{x}_{ij:}$, respectively. A **slice** is a two-dimensional section of a tensor, defined by fixing all, but two indices. The horizontal, lateral, and frontal slides of a third-order tensor \mathcal{X} , denoted by $\mathbf{X}_{i::}$, $\mathbf{X}_{::j:}$, and $\mathbf{X}_{::k:}$, respectively. The mode- n matricization of a tensor $\mathcal{X} \in \mathbb{R}^{I_1 \times I_2 \times \dots \times I_N}$ is denoted by $\mathbf{X}_{(n)}$ and arranges the mode- n fibers to be the columns of the resulting matrix [37].

The inner product of two same-dimensional tensors \mathcal{X} and \mathcal{Y} is defined as $\langle \mathcal{X}, \mathcal{Y} \rangle := \sum_{i_1, i_2, \dots, i_N} x_{i_1, i_2, \dots, i_N} \cdot y_{i_1, i_2, \dots, i_N}$. The corresponding norm (Frobenius norm) is defined as $\|\mathcal{X}\|_F := \sqrt{\langle \mathcal{X}, \mathcal{X} \rangle}$. In addition, the ℓ_1 norm is calculated as $\|\mathcal{X}\|_1 := \sum_{i_1, i_2, \dots, i_N} |x_{i_1, i_2, \dots, i_N}|$. The n -mode product of a tensor with a matrix is calculated as $(\mathcal{X} \times_n \mathbf{U})_{i_1, \dots, i_{n-1}, i_{n+1}, \dots, i_N} = \sum_{i_n} x_{i_1, i_2, \dots, i_N} \cdot u_{j, i_n}$. The multilinear rank is defined as an array (r_1, r_2, \dots, r_I) , where $r_n = \text{rank}(\mathbf{X}_{(n)})$, $n = 1, 2, \dots, N$. For a more detailed introduction of tensor, please refer to [37].

III. PROPOSED METHOD

A. Problem Formulation

Assuming that the striping effects in MSI are considered to be additive noise, then the degradation model of stripe noise

removal can be expressed as

$$\mathcal{Y} = \mathcal{X} + \mathcal{S} + \mathcal{N} \quad (1)$$

where \mathcal{Y} , \mathcal{X} , \mathcal{S} , and \mathcal{N} are third-order tensors representing the degraded image, the clean image (or image component), the stripe component, and the noise (or error) term, respectively. The size of \mathcal{Y} , \mathcal{X} , \mathcal{S} , and \mathcal{N} is $M \times N \times B$, in which M and N , respectively, denote the number of rows and columns of the image in each band, and B stands for the number of bands.

The goal of this paper is to separate the image component \mathcal{X} and stripe component \mathcal{S} from the degraded image \mathcal{Y} , as shown in Fig. 1(a). However, the issue of directly computing \mathcal{X} and \mathcal{S} from \mathcal{Y} is an ill-posed problem. For this ill-posed problem, regularization is an effective tool to guarantee the stable solution. Thus, the corresponding destriping objective function can be formulated as follows:

$$\min_{\mathcal{X}, \mathcal{S}} \frac{1}{2} \|\mathcal{Y} - \mathcal{X} - \mathcal{S}\|_F^2 + \alpha_1 J_1(\mathcal{X}) + \alpha_2 J_2(\mathcal{S}) \quad (2)$$

where the first term is the data-fidelity term; $J_1(\mathcal{X})$ and $J_2(\mathcal{S})$ are the regularization terms, which describe the prior information of the image component and stripe component, respectively. α_1 and α_2 are the positive regularization parameters, which is used to balance the three terms. Therefore, to effectively separate the image component and stripe component from the degraded image, the key problem is that we need to exploit the prior information for both \mathcal{X} and \mathcal{S} and then design corresponding regularizers, which will be discussed in the next subsection.

B. Priors and Regularizers

In this subsection, we will introduce how to design efficient regularizers for \mathcal{X} and \mathcal{S} in detail, respectively.

1) *Spatial Correlation of the Stripe Component*: From the perspective of linear mixture model, it is well known that HSI has a strong correlation in spectral dimension, based on the assumption that each spectral signature can be represented by a linear combination of few pure spectral endmembers. Since the MSI can be regarded as a part of bands in HSI, the spectral correlation also exists in MSI, which implies that the mode-3 unfolding matrix $\mathbf{X}_{(3)}$ can be approximated by a matrix factorization $\mathbf{X}_{(3)} = \mathbf{V}_3 \mathbf{C}_3$, where \mathbf{V}_3 is a low-rank matrix (i.e., the column of \mathbf{V}_3 is much less than $\mathbf{X}_{(3)}$). However, the correlation is weak in both spatial dimensions for MSI. We can measure these properties by using an example. One $256 \times 256 \times 10$ subimage from *Washington DC Mall Data* is shown in Fig. 1(a-2), and the distributions of the normalized singular value of the unfolding matrices in both spatial dimensions (i.e., mode 1 and mode 2 directions) are shown in Fig. 1(b-2) and (b-3). From Fig. 1(b-2) and (b-3), we can see that the singular value curves have decaying trends, but the trend of falling to zero is very slow. The weak spatial correlation in MSI indicates that the matrix unfoldings $\mathbf{X}_{(1)}$ and $\mathbf{X}_{(2)}$ in both two spatial modes can be approximated by two high-rank matrices, respectively. Mathematically, $\mathbf{X}_{(1)} = \mathbf{V}_1 \mathbf{C}_1$ and $\mathbf{X}_{(2)} = \mathbf{V}_2 \mathbf{C}_2$, where \mathbf{V}_1 and \mathbf{V}_2 are two high-rank matrices. Based on these priors of the spatial-spectral correlation of the tensor data and the popular Tucker decomposition in multilinear algebra [35], [36], the

low-rank Tucker decomposition can be introduced to aggregate the matrix factorizations above as follows:

$$\mathcal{X} = \mathcal{C} \times_1 \mathbf{V}_1 \times_2 \mathbf{V}_2 \times_3 \mathbf{V}_3.$$

However, in our work, we utilize low-rank Tucker decomposition to constrain the stripe component \mathcal{S} rather than the image component \mathcal{X} , the main reason is that the correlation of stripe component in both spatial dimensions is stronger than the image component.

We can explain this strategy using the low-rank Tucker decomposition for stripe component from quantitatively perspective. Fig. 1(a-3) shows the simulated stripe component, which is generated following the experiments in [26]. Then, we also give the distributions of the normalized singular value of the unfolding matrices for the stripe component in both spatial dimensions, which are shown in Fig. 1(c-2) and (c-3). Compared with Fig. 1(b-2) and (b-3), we can find that the singular values distributions of mode-1 and mode-2 unfolding matrices are falling faster than the image component. In particular, the singular values of mode-1 unfolding matrix [see Fig. 1(c-2)] rapidly decrease to zero with rank 1, whereas the singular values of the image component [see Fig. 1(b-2)] slowly decrease to zero with rank close to 100. From Fig. 1(b-3) and (c-3), the singular values also decrease to zero faster than the image component. To sum up, compared with the image component, the strong spatial correlation in stripe component implies that the matrix unfoldings $\mathbf{S}_{(1)} \in R^{M \times N \times B}$ and $\mathbf{S}_{(2)} \in R^{N \times M \times B}$ in both the spatial modes can be factorized two low-rank matrices, respectively. Mathematically, $\mathbf{S}_{(1)} = \mathbf{U}_1 \mathbf{G}_1$ and $\mathbf{S}_{(2)} = \mathbf{U}_2 \mathbf{G}_2$, where $\mathbf{U}_1 \in R^{M \times r_1}$, $\mathbf{U}_2 \in R^{N \times r_2}$, $r_1 \ll M$ and $r_2 \ll N$. Since we assume that the locations of the stripe component are randomly distributed in each band, the weak spectral correlation implies that the matrix unfolding $\mathbf{S}_{(3)} \in R^{B \times M \times N}$ can be approximated by a high-rank matrix, i.e., $\mathbf{S}_{(3)} = \mathbf{U}_3 \mathbf{G}_3$, where $\mathbf{U}_3 \in R^{B \times r_3}$ and $r_3 \leq B$. This phenomenon demonstrates that using low-rank Tucker decomposition regularization to constrain the stripe component is more reasonable than the image component. Therefore, the above can be formulated together as follows:

$$\mathcal{S} = \mathcal{G} \times_1 \mathbf{U}_1 \times_2 \mathbf{U}_2 \times_3 \mathbf{U}_3 \quad (3)$$

where $\mathbf{U}_1 \in R^{M \times r_1}$, $\mathbf{U}_2 \in R^{N \times r_2}$, and $\mathbf{U}_3 \in R^{B \times r_3}$ are the factor matrices, which are orthogonal in columns for two spatial modes and spectral mode, respectively. The tensor $\mathcal{G} \in R^{r_1 \times r_2 \times r_3}$ is named core tensor.

Compared to the band-by-band low-rank matrix modeling regularization [26], [33], the advantages of our LRTD modeling strategy are that it can simultaneously encode the high correlation of the stripe component in both spatial correlations. Thus it can more precisely extract the stripe component \mathcal{S} .

2) *Group Sparsity of the Stripe Component*: From Fig. 1(a-3), we can observe that the stripe component presents a special line pattern characteristic in each band compared with other forms of noise (such as Gaussian noise and impulse noise). In [24], the authors used ℓ_0 norm to constrain the stripe component because the stripe component can be considered as a sparse matrix with a plenty of zero elements in the stripe-free locations. However,

the sparsity prior of ℓ_0 loss assumes that the sparse elements are randomly distributed, and it fails to consider the inner structure among these elements. Intuitively, the stripe component consists of the stripe column and stripe-free column, and each column can be viewed as a group. Moreover, the pixel values of stripe-free column tend to be all zeros, and the stripe columns are all nonzeros. Based on this property, the stripe component can approximately be considered as being group sparsity when the stripe noise is not heavy. To enhance the group sparsity of the stripe component, using $\ell_{2,0}$ norm of the stripe component \mathcal{S} is an ideal option since the $\ell_{2,0}$ norm promotes the number of nonzero lines (the column fibers) of \mathcal{S} . However, due to the NP-hard problem of $\ell_{2,0}$, we settle for introducing $\ell_{2,1}$ norm to describe the group sparse prior [22], [28]. To do this, we finally construct the other one regularization for the stripe component as

$$J_2(\mathcal{S}) = \|\mathcal{S}\|_{2,1} \quad (4)$$

where $\|\mathcal{S}\|_{2,1} = \sum_{k=1}^B \sum_{j=1}^N \sqrt{\sum_{i=1}^M (x_{ijk})^2}$.

3) Piecewise Smoothness of the Image Component in Spatial-Spectral Directions: Unlike other forms of noise, the stripe noise usually presents special directional feature (i.e., horizontal or vertical). In our study, we consider each stripe line as a vertical. If the stripes are horizontal, we rotate them to make the stripe lines vertical. To describe the special directional feature of the stripe noise, we present the derivation images in spatial-spectral directions for the degraded image and clean image, respectively. The derivation images of the spatial horizontal, spatial vertical, and spectral directions of these two images are shown in Fig. 1(d-2), (d-3), and (d-4), and Fig. 1(d-6), (d-7), and (d-8), respectively. From Fig. 1(d-2), (d-3), and (d-4) to see, the three derivation images are very smooth and sparse, which indicates that the image component has a piecewise smooth prior in the spatial-spectral directions. However, due to the existence of the stripe noise, the smoothness of the spatial horizontal derivation and spectral derivation are seriously destroyed as shown in Fig. 1(d-6) and (d-8), whereas the spatial vertical derivation also preserves the smooth structure. Based on these observations, it motivates us to design a regularization, which can fully preserve the piecewise smoothness of the image in both spatial horizontal and spectral directions so as to remove the stripe noise from the image component. In recent, the TV regularization is an efficient method to preserve the piecewise smooth structure in the image [38]–[40]. Naturally, a spatial horizontal unidirectional TV regularization and the spectral TV regularization are introduced to promote the smooth structure. Thus, the final regularizer for the image component is given as follows:

$$J_1(\mathcal{X}) = \lambda_1 \|D_x \mathcal{X}\|_1 + \lambda_2 \|D_z \mathcal{X}\|_1 \quad (5)$$

where D_x and D_z are the spatial horizontal and spectral differential operators, respectively. Let $\mathcal{X}(i, j, k)$ represent the intensity at the location (i, j, k) , then the differential operators are defined by

$$\begin{cases} D_x \mathcal{X}(i, j, k) = \mathcal{X}(i, j+1, k) - \mathcal{X}(i, j, k) \\ D_z \mathcal{X}(i, j, k) = \mathcal{X}(i, j, k+1) - \mathcal{X}(i, j, k). \end{cases}$$

C. Proposed Model

After fully exploiting the prior knowledge of the stripe component and image component and designing the corresponding regularizers, we now can instantiate the destriping objective function in (2). Combining the modeling of the stripe component in (3) and (4) and the image component in (5) into the regularization model in (2), we can obtain the final minimization model for solving the destriping of MSI as follows:

$$\begin{aligned} \min_{\mathcal{X}, \mathcal{S}, \mathcal{G}, \mathbf{U}_i} \quad & \frac{1}{2} \|\mathcal{Y} - \mathcal{X} - \mathcal{S}\|_F^2 + \lambda_1 \|D_x \mathcal{X}\|_1 + \lambda_2 \|D_z \mathcal{X}\|_1 \\ & + \lambda_3 \|\mathcal{S}\|_{2,1} \\ \text{s.t. } \quad & \mathcal{S} = \mathcal{G} \times_1 \mathbf{U}_1 \times_2 \mathbf{U}_2 \times_3 \mathbf{U}_3, \quad \mathbf{U}_i^T \mathbf{U}_i = \mathbf{I} \quad (i = 1, 2, 3) \end{aligned} \quad (6)$$

where λ_1 , λ_2 , and λ_3 are three positive regularization parameters.

It should be noted that the proposed model can effectively use the image decomposition framework to simultaneously capture the prior information of the stripe component and image component, and thus is expected to have a strong ability of accurately separating the stripe component and image component. More specifically, the two spatial mode correlation of all the stripe component pixels and the certain correlations in spectral mode can be well captured by the low-rank Tucker decomposition. Moreover, the group sparsity regularization can be used to maintain the line pattern of the stripe component. Though when the stripes are very heavy, it seems that this regularization is not proper. However, the group sparsity term also can be viewed as a role to restrain the magnitude and structure of stripes. Meanwhile, we can tune the parameters of the model to handle a scene with heavy stripes. For the image component, the designed TV regularization in spatial horizontal and spectral directions are used to suppress the stripes in the spatial domain and preserve the spectral consistency.

D. Optimization Procedure

Clearly, due to the nonconvexity of the low-rank Tucker decomposition, the proposed model is a nonconvex optimization problem, and then we can only expect to find a local optimal solution. For efficiency, we develop an efficient algorithm based on ALM method [36], [41] to optimize the proposed model in (6). The implementation details of our optimization algorithms are presented in the following.

By introducing three auxiliary variables, the proposed model in (6) can be rewritten as the following equivalent problem:

$$\begin{aligned} \min_{\mathcal{X}, \mathcal{S}, \mathcal{G}, \mathbf{U}_i, \mathcal{R}_1, \mathcal{R}_2, \mathcal{Q}} \quad & \frac{1}{2} \|\mathcal{Y} - \mathcal{X} - \mathcal{S}\|_F^2 + \lambda_1 \|\mathcal{R}_1\|_1 \\ & + \lambda_2 \|\mathcal{R}_2\|_1 + \lambda_3 \|\mathcal{Q}\|_{2,1} \\ \text{s.t. } \quad & \mathcal{R}_1 = D_x \mathcal{X}, \quad \mathcal{R}_2 = D_z \mathcal{X}, \quad \mathcal{Q} = \mathcal{S} \\ & \mathcal{S} = \mathcal{G} \times_1 \mathbf{U}_1 \times_2 \mathbf{U}_2 \times_3 \mathbf{U}_3, \quad \mathbf{U}_i^T \mathbf{U}_i = \mathbf{I} \quad (i = 1, 2, 3). \end{aligned} \quad (7)$$

Then, by applying the ALM method, the augmented Lagrangian function of problem (7) is

$$\begin{aligned} L_\beta(\mathcal{X}, \mathcal{S}, \mathcal{G}, \mathbf{U}_i, \mathcal{R}_1, \mathcal{R}_2, \mathcal{Q}, \mathcal{W}_i) = & \frac{1}{2} \|\mathcal{Y} - \mathcal{X} - \mathcal{S}\|_F^2 \\ & + \lambda_1 \|\mathcal{R}_1\|_1 + \lambda_2 \|\mathcal{R}_2\|_1 + \lambda_3 \|\mathcal{Q}\|_{2,1} + \frac{\beta}{2} \left\| \mathcal{R}_1 - D_x \mathcal{X} \right. \\ & \left. + \frac{\mathcal{W}_1}{\beta} \right\|_F^2 + \frac{\beta}{2} \left\| \mathcal{R}_2 - D_z \mathcal{X} + \frac{\mathcal{W}_2}{\beta} \right\|_F^2 + \frac{\beta}{2} \left\| \mathcal{Q} - \mathcal{S} + \frac{\mathcal{W}_3}{\beta} \right\|_F^2 \end{aligned} \quad (8)$$

under the Tucker decomposition constraints $\mathcal{S} = \mathcal{G} \times_1 \mathbf{U}_1 \times_2 \mathbf{U}_2 \times_3 \mathbf{U}_3$, $\mathbf{U}_i^T \mathbf{U}_i = \mathbf{I}$ ($i = 1, 2, 3$), where \mathcal{W}_i ($i = 1, 2, 3$) are the scaled Lagrange multipliers, and β is a positive penalty parameter. It is hard to simultaneously solve all these variables, thus we can approximately and alternatively optimize the problem (8) over one variable with the other variables fixed. Therefore, we take advantage of the optimization algorithm to separate the difficult optimization problem (8) into the following easy subproblems.

1) \mathcal{R}_1 subproblem: By fixing the other variables, the optimization problem \mathcal{R}_1 is given by

$$\arg \min_{\mathcal{R}_1} \lambda_1 \|\mathcal{R}_1\|_1 + \frac{\beta}{2} \left\| \mathcal{R}_1 - D_x \mathcal{X} + \frac{\mathcal{W}_1}{\beta} \right\|_F^2$$

which can be efficiently solved by the following soft-threshold shrinkage operator [42]

$$\mathcal{R}_1 = \text{soft} \left(D_x \mathcal{X} - \frac{\mathcal{W}_1}{\beta}, \frac{\lambda_1}{\beta} \right) \quad (9)$$

where $\text{soft}(r, \theta) = \text{sgn}(r) * \max(|r| - \theta, 0)$.

2) \mathcal{R}_2 subproblem: Similarly to the \mathcal{R}_1 subproblem, the \mathcal{R}_2 subproblem is also obtained by the soft-threshold shrinkage operator, i.e.,

$$\begin{aligned} \arg \min_{\mathcal{R}_2} \lambda_2 \|\mathcal{R}_2\|_1 + \frac{\beta}{2} \left\| \mathcal{R}_2 - D_z \mathcal{X} + \frac{\mathcal{W}_2}{\beta} \right\|_F^2 \\ \mathcal{R}_2 = \text{soft} \left(D_z \mathcal{X} - \frac{\mathcal{W}_2}{\beta}, \frac{\lambda_2}{\beta} \right). \end{aligned} \quad (10)$$

3) \mathcal{Q} subproblem: Minimizing (8) with respect to \mathcal{Q} can be solved by

$$\arg \min_{\mathcal{Q}} \lambda_3 \|\mathcal{Q}\|_{2,1} + \frac{\beta}{2} \left\| \mathcal{Q} - \mathcal{S} + \frac{\mathcal{W}_3}{\beta} \right\|_F^2.$$

Let $\mathcal{S} - \frac{\mathcal{W}_3}{\beta} = \mathcal{B}$, then the optimal solution of column fibers of \mathcal{Q} is given as (see [43])

$$\begin{aligned} \mathcal{Q}(:, j, k) = & \\ & \begin{cases} \frac{\|\mathcal{B}(:, j, k)\| - \frac{\lambda_3}{\beta}}{\|\mathcal{B}(:, j, k)\|} \mathcal{B}(:, j, k), & \text{if } \frac{\lambda_3}{\beta} < \|\mathcal{B}(:, j, k)\| \\ 0, & \text{otherwise.} \end{cases} \end{aligned} \quad (11)$$

4) \mathcal{S} , \mathcal{G} , and \mathbf{U}_i subproblems: By keeping the other variables fixed, the optimization problems of \mathcal{S} , \mathcal{G} , and \mathbf{U}_i are given by:

$$\min_{\substack{\mathbf{U}_i^T \mathbf{U}_i = \mathbf{I}, \\ \mathcal{S} = \mathcal{G} \times_1 \mathbf{U}_1 \times_2 \mathbf{U}_2 \times_3 \mathbf{U}_3}} \frac{1}{2} \|\mathcal{Y} - \mathcal{X} - \mathcal{S}\|_F^2 + \frac{\beta}{2} \left\| \mathcal{Q} - \mathcal{S} + \frac{\mathcal{W}_3}{\beta} \right\|_F^2$$

which can be combined into the following equivalent formula:

$$\begin{aligned} \min_{\mathbf{U}_i^T \mathbf{U}_i = \mathbf{I}} & \frac{1 + \beta}{2} \left\| \mathcal{G} \times_1 \mathbf{U}_1 \times_2 \mathbf{U}_2 \times_3 \mathbf{U}_3 \right. \\ & \left. - \frac{(\mathcal{Y} - \mathcal{X}) + \beta(\mathcal{Q} + \frac{\mathcal{W}_3}{\beta})}{1 + \beta} \right\|_F^2. \end{aligned} \quad (12)$$

The variables \mathcal{G} and \mathbf{U}_i can be effectively solved by using the classic HOOI algorithm [37], then we update the \mathcal{S} subproblem as follows:

$$\mathcal{S} = \mathcal{G} \times_1 \mathbf{U}_1 \times_2 \mathbf{U}_2 \times_3 \mathbf{U}_3. \quad (13)$$

5) \mathcal{X} subproblem: The \mathcal{X} subproblem is a least-squared problem

$$\begin{aligned} \arg \min_{\mathcal{X}} & \frac{1}{2} \|\mathcal{Y} - \mathcal{X} - \mathcal{S}\|_F^2 + \frac{\beta}{2} \left\| \mathcal{R}_1 - D_x \mathcal{X} + \frac{\mathcal{W}_1}{\beta} \right\|_F^2 \\ & + \frac{\beta}{2} \left\| \mathcal{R}_2 - D_z \mathcal{X} + \frac{\mathcal{W}_2}{\beta} \right\|_F^2 \end{aligned}$$

which is equivalent to solve the following linear system:

$$\begin{aligned} (\mathcal{I} + \beta D_x^T D_x + \beta D_z^T D_z) \mathcal{X} = & (\mathcal{Y} - \mathcal{S}) \\ & + \beta D_x^T \left(R_1 + \frac{\mathcal{W}_1}{\beta} \right) + \beta D_z^T \left(R_2 + \frac{\mathcal{W}_2}{\beta} \right) \end{aligned}$$

where \mathcal{I} is the unit tensor. In this work, we consider the periodic boundary condition for \mathcal{X} , then $D_x^T D_x$ and $D_z^T D_z$ are block circulant matrices with circulant blocks; thus it can be efficiently solved by the fast Fourier transform (FFT)

$$\mathcal{X} = \text{ifftn} \left(\frac{\mathcal{A}}{\beta \mathbf{1} + \beta(|\text{fftn}(D_x)|^2 + |\text{fftn}(D_z)|^2)} \right) \quad (14)$$

where $\mathcal{A} = \text{fftn}((\mathcal{Y} - \mathcal{S}) + \beta D_x^T (R_1 + \frac{\mathcal{W}_1}{\beta}) + \beta D_z^T (R_2 + \frac{\mathcal{W}_2}{\beta}))$, fftn and ifftn are the fast 3-D Fourier transform and its inverse transform, $|\cdot|^2$ is the element-wise square, and the division is also performed element-wisely.

6) Multipliers updating: According to the solved algorithm, the Lagrange multipliers \mathcal{W}_i ($i = 1, 2, 3$) can be updated as follows:

$$\begin{cases} \mathcal{W}_1 = \mathcal{W}_1 + \beta(\mathcal{R}_1 - D_x \mathcal{X}) \\ \mathcal{W}_2 = \mathcal{W}_2 + \beta(\mathcal{R}_2 - D_z \mathcal{X}) \\ \mathcal{W}_3 = \mathcal{W}_3 + \beta(\mathcal{Q} - \mathcal{S}) \end{cases} \quad (15)$$

Combining the above solved subproblems, we have a one-step iteration for solving the algorithm. The proposed method for the MSI stripe noise removal can be summarized in Algorithm 1.

E. Analysis of Computational Complexity

Here, we will analyze the computational complexity of our algorithm. The computation of Algorithm 1 involves the

Algorithm 1: The Optimization Procedure for the Proposed Model.

Input: The degraded image $\mathcal{Y} \in R^{M \times N \times B}$, the estimated rank (r_1, r_2, r_3) for Tucker decomposition, the parameters $\lambda_1, \lambda_2, \lambda_3, \beta, \varepsilon, k_{\max}$.

- 1: Initialize: Set $\mathcal{X} = \mathcal{Y}, \mathcal{R}_1 = \mathcal{R}_2 = \mathcal{Q} = \mathcal{S} = \mathcal{W}_1 = \mathcal{W}_2 = \mathcal{W}_3 = \mathbf{0}, k = 0$.
- 2: **while** stopping criterion is not satisfied **do**
- 3: Update \mathcal{R}_1 and \mathcal{R}_2 using a soft-threshold shrinkage method by (9) and (10), respectively.
- 4: Update \mathcal{Q} via (11).
- 5: Compute \mathcal{G} , \mathbf{U}_i and \mathcal{S} by (12) and (13).
- 6: Compute \mathcal{X} via a linear system (14).
- 7: Update the three Lagrange multipliers $\mathcal{W}_1, \mathcal{W}_2$ and \mathcal{W}_3 by (15).
- 8: Check the convergence condition $\frac{\|\mathcal{X}^{k+1} - \mathcal{X}^k\|_F}{\|\mathcal{X}^k\|_F} \leq \varepsilon$ and $k < k_{\max}$.
- 9: **end while**

Output: The estimations of the stripe-free MSI \mathcal{X} and the stripe component \mathcal{S} .

threshold shrinkage, HOOI algorithm, and FFT operation. The \mathcal{R}_1 , \mathcal{R}_2 , and \mathcal{Q} subproblems are solved by threshold shrinkage operations, thus the complexity for each subproblem is $O(MNB)$. The \mathcal{S} , \mathcal{G} , and \mathbf{U}_i subproblems involve the HOOI algorithm, which comes from computing the SVDs and forming the tensor-matrix product. For simplicity, we denote $r = \max\{r_1, r_2, r_3\}$, then the total cost for one iteration of HOOI is $O(MNBr + (M + N + B)r^4 + r^6)$ [44]. In addition, the \mathcal{X} subproblem is solved by FFT, which requires $O(MNB \log(MNB))$ operations. Thus, the total computational complexity of algorithm 1 is $O(3MNB + MNBr + (M + N + B)r^4 + r^6 + MNB \log(MNB))$.

IV. EXPERIMENTAL RESULTS AND DISCUSSION

In this section, we employ both simulated and real data experiments to verify the effectiveness of the proposed method for MSI stripe noise removal. We compare our method with three recent state-of-the-art methods, including anisotropic spectral-spatial TV (ASSTV) model [32], image decomposition based band-by-band low-rank regularization and spatial-spectral TV model (LRMD) [26], and TV regularization and group sparsity constraint method (TVGS) [27]. The implementation codes of ASSTV and LRMD can be directly obtained from the author's homepage,¹ and TVGS is our recent work. For the reproduction of our research, we will publish our code in the author's homepage.² In the following experiments, the parameters in those three compared methods are manually tuned according to the author's rules in their paper to guarantee their possibly good performance. For the parameters of our LRTD method, we would like to show the detailed discussion in Section IV-C. All of the experiments are implemented in MATLAB R2017b on a

desktop of 16 GB RAM, Intel (R) Core (TM) i7-8700K CPU, @3.70 GHz.

A. Simulated Data Experiments

In the simulated experiments, the Washington DC Mall, which can be downloaded on website,³ is selected as the ground-truth image. The original Washington DC Mall contains 191 spectral bands with 1208×307 pixels in each band, and we extract a subimage of size $256 \times 256 \times 10$ in our experiment. In our experiments, we simulate two types of stripes according to the distribution of the stripe location in different bands. To better the numerical calculation and visualization, the gray values of the MSI are scaled to $[0, 1]$ before adding stripes.

1) Locations of Stripes are Randomly Distributed in Each Band

In this type of experiment, we choose the Washington DC Mall subimage as the ground truth to add stripes. In remote sensing imaging systems, there are mainly two kinds of stripe noise in an image: Periodic stripes in cross-track imaging devices and nonperiodic stripes in push-broom imaging devices. To simulate these cases, we, respectively, consider the periodic and nonperiodic stripes to the ground-truth image, and the locations of stripes are randomly distributed in each band. To make the situation more complicated, the degradation levels of the different stripe lines are also different. Both the periodic and nonperiodic stripes are added in the following pattern based on the degradation model (1).

Stripe noise generation: Adding stripes to an image is indeed an open problem, since there is no unified method, thus we can synthetic stripes following the recent stripe noise removal literature [26]. Before adding stripes to the image, we need to determine two indicators: the percentage of the stripe area within the image (denote r), and the intensity (mean absolute value of pixels) of each stripe line (denote I). The percentage r of stripes in the set of $\{0.2, 0.5, 0.8, 0 - 1\}$ are considered in our experiment. Meanwhile, the intensity I of each stripe line in the set of $\{0.2, 0.5, 0.8, 0 - 1\}$ are added to the image. It is worth noting that $r = 0 - 1$ represents that the degradation percentage of the stripe lines is different in each band. Similarly, $I = 0 - 1$ denotes that the intensity of each stripe line is randomly distributed. For simulating periodic stripes, $r \times 10$ stripe lines in every ten lines are periodically added into the image and the intensity value of each stripe line equal to I . We randomly select $r * N$ lines in the image to add stripes for simulating nonperiodic stripes. Therefore, we, respectively, simulate 16 different cases for periodic and nonperiodic stripes, which makes the situation more complicated.

Visual quality comparison: Since there are many degraded cases in our simulated experiment, we choose one case from the periodic stripes and nonperiodic stripe experiment for comparison, respectively. Moreover, because of the page limitation, we only present one typical band of the simulated data before and after destriping. Fig. 2 shows the results of the different destriping methods with the periodic stripes in case of $r = 0.5$ and

¹<http://www.escience.cn/people/changyi/index.html>

²https://www.researchgate.net/profile/Yong_Chen96

³<https://engineering.purdue.edu/biehl/MultiSpec/hyperspectral.html>

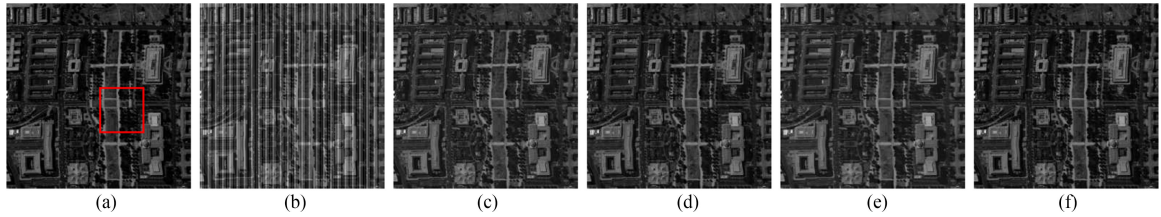


Fig. 2. Destriping results of band 10 for the periodic stripes case ($r = 0.5$ and $I = 0.2$). (a) Original. (b) Degraded image with periodic stripes. Destriping results of (c) ASSTV, (d) LRMID, (e) TVGS, (f) LRTD.

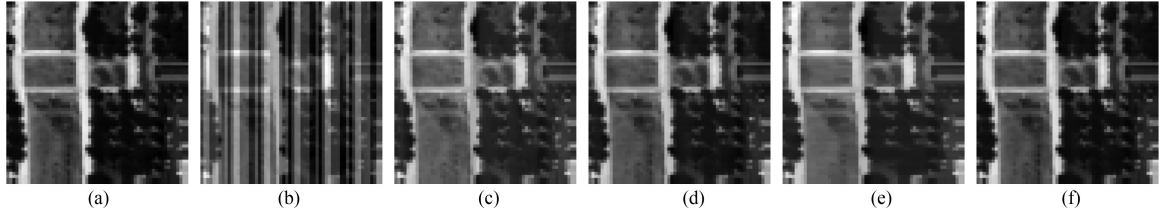


Fig. 3. Magnified results of Fig. 2. (a) Original. (b) Degraded image with periodic stripes. Destriping results of (c) ASSTV, (d) LRMID, (e) TVGS, (f) LRTD.

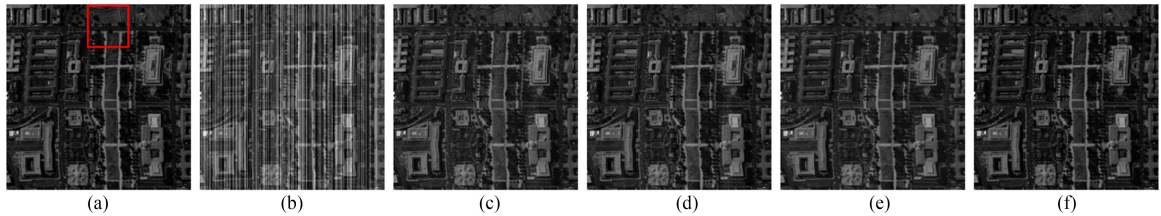


Fig. 4. Destriping results of band 5 for the nonperiodic stripes case ($r = 0.5$ and $I = 0.2$). (a) Original. (b) Degraded image with nonperiodic stripes. Destriping results of (c) ASSTV, (d) LRMID, (e) TVGS, (f) LRTD.

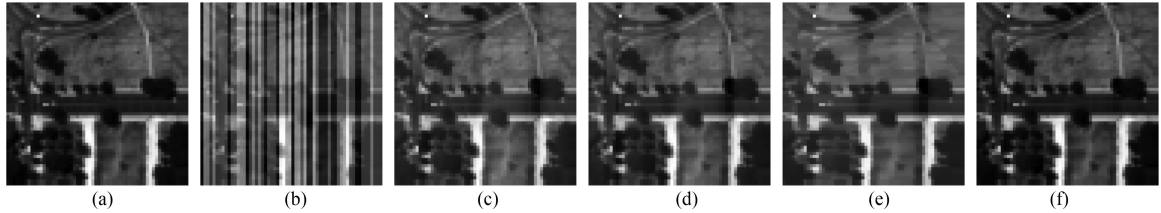


Fig. 5. Magnified results of Fig. 4. (a) Original. (b) Degraded image with nonperiodic stripes. Destriping results of (c) ASSTV, (d) LRMID, (e) TVGS, (f) LRTD.

$I = 0.2$. Fig. 2(a) presents the original band 10 in our selected Washington DC Mall data. The image is seriously contaminated by the stripe noise, as shown in Fig. 2(b). The destriping results of the compared methods are shown in Fig. 2(c)–(f). Similarly, the results of nonperiodic stripe case ($r = 0.5$ and $I = 0.2$) are shown in Fig. 4. For better visual comparison, we magnify some detailed regions cropped from the image. Figs. 3 and 5 display the magnified results of the red box subregion in Figs. 2 and 4, respectively. From Figs. 2 to 5(c)–(e), it can be seen that ASSTV, LRMID, and TVGS can remove all of the obvious stripes. However, these methods fail to preserve the detailed information, which results in image distortion, blur, and over smoothness. For example, Fig. 3(c) and (e) shows the subregion results of ASSTV and TVGS, respectively; it is obvious that the trees are completely oversmoothed and blurred in the image,

and the similar observation can be observed in Fig. 5(c) and (e). As shown in Figs. 3–5(d), LRMID also obtains the minor distortion compared with ASSTV and TVGS. Unfortunately, it introduces some stripe-like artifacts as shown in Fig. 5(d). From the results of the proposed method shown in Figs. 2–5(f), it can be clearly seen that the proposed LRTD model achieves the best destriping reconstruction results. In particular, we can observe the superiority of LRTD from magnified results Figs. 3(f) and 5(f), which show that the proposed LRTD can effectively remove stripes and preserve image details and structures.

Quantitative comparison: To further evaluate the overall performance of the proposed method, we give the quantitative comparison for all experimental cases. Since the ground-truth image exists, three quantitative indices, i.e., the mean peak signal-to-noise ratio (MPSNR), mean structural similarity (MSSIM) [45],

TABLE I
QUANTITATIVE EVALUATION OF THE DIFFERENT METHODS FOR PERIODIC STRIPES UNDER DIFFERENT NOISE LEVELS ON WASHINGTON DC MALL DATA

r	I	Index	Degrade	ASSTV	LRMID	TVGS	LRTD	r	I	Index	Degrade	ASSTV	LRMID	TVGS	LRTD
0.2	MPSNR	21.07	38.04	39.12	44.79	49.66		0.5	MPSNR	17.09	32.23	33.08	35.93	43.90	
	MSSIM	0.553	0.986	0.990	0.995	0.998			MSSIM	0.296	0.974	0.979	0.975	0.996	
	MSAM	0.455	0.032	0.045	0.024	0.025			MSAM	0.749	0.047	0.045	0.019	0.035	
	MPSNR	13.11	35.87	37.23	39.21	49.68			MPSNR	9.13	25.77	25.71	34.00	44.13	
	MSSIM	0.242	0.980	0.987	0.981	0.998			MSSIM	0.047	0.906	0.902	0.971	0.996	
	MSAM	0.814	0.047	0.052	0.029	0.025			MSAM	1.177	0.062	0.063	0.039	0.035	
	MPSNR	9.03	34.54	36.24	39.22	49.68			MPSNR	5.05	21.87	21.89	33.07	42.78	
	MSSIM	0.134	0.975	0.985	0.981	0.998			MSSIM	0.011	0.745	0.743	0.959	0.994	
	MSAM	0.991	0.048	0.052	0.029	0.025			MSAM	1.343	0.319	0.324	0.028	0.041	
	MPSNR	11.79	34.95	36.27	39.47	49.73			MPSNR	7.68	24.66	24.83	34.12	44.42	
0.8	MSSIM	0.263	0.981	0.988	0.981	0.999		0.1	MSSIM	0.082	0.881	0.883	0.955	0.996	
	MSAM	0.81	0.047	0.047	0.032	0.025			MSAM	1.211	0.127	0.121	0.077	0.033	
0.5	MPSNR	15.05	37.49	38.86	37.00	39.78		0.8	MPSNR	19.61	35.91	42.48	40.61	47.55	
	MSSIM	0.213	0.987	0.991	0.977	0.992			MSSIM	0.463	0.987	0.995	0.959	0.998	
	MSAM	0.798	0.047	0.045	0.069	0.042			MSAM	0.588	0.047	0.038	0.101	0.029	
	MPSNR	7.09	35.19	36.91	35.59	38.92			MPSNR	11.65	28.58	41.59	36.91	47.46	
	MSSIM	0.035	0.979	0.986	0.973	0.991			MSSIM	0.189	0.952	0.994	0.969	0.998	
	MSAM	1.154	0.048	0.047	0.037	0.042			MSAM	1.013	0.048	0.050	0.059	0.029	
	MPSNR	3.01	33.85	34.39	34.71	38.10			MPSNR	7.56	24.88	42.70	36.11	46.23	
	MSSIM	0.011	0.970	0.969	0.968	0.990			MSSIM	0.106	0.886	0.995	0.966	0.997	
	MSAM	1.281	0.050	0.048	0.037	0.050			MSAM	1.208	0.074	0.047	0.057	0.036	
	MPSNR	5.85	29.27	30.04	30.04	38.95			MPSNR	10.31	27.23	40.09	35.40	48.88	
0.1	MSSIM	0.051	0.954	0.954	0.919	0.991		0.1	MSSIM	0.234	0.935	0.992	0.926	0.998	
	MSAM	1.195	0.054	0.075	0.250	0.048			MSAM	1.020	0.062	0.049	0.150	0.029	

TABLE II
QUANTITATIVE EVALUATION OF THE DIFFERENT METHODS FOR NONPERIODIC STRIPES UNDER DIFFERENT NOISE LEVELS ON WASHINGTON DC MALL DATA

r	I	Index	Degrade	ASSTV	LRMID	TVGS	LRTD	r	I	Index	Degrade	ASSTV	LRMID	TVGS	LRTD
0.2	MPSNR	20.98	37.14	38.08	37.25	49.07		0.5	MPSNR	16.98	34.77	34.72	35.06	44.41	
	MSSIM	0.597	0.988	0.991	0.978	0.998			MSSIM	0.325	0.982	0.983	0.974	0.997	
	MSAM	0.469	0.047	0.044	0.019	0.026			MSAM	0.709	0.047	0.046	0.061	0.035	
	MPSNR	13.02	33.48	33.41	37.31	49.05			MPSNR	9.03	30.03	31.44	32.10	42.44	
	MSSIM	0.319	0.977	0.969	0.979	0.998			MSSIM	0.070	0.958	0.959	0.956	0.996	
	MSAM	0.831	0.047	0.052	0.025	0.026			MSAM	1.099	0.048	0.060	0.090	0.048	
	MPSNR	8.94	30.82	31.75	34.86	48.57			MPSNR	4.94	28.67	30.06	27.82	42.45	
	MSSIM	0.228	0.966	0.964	0.966	0.998			MSSIM	0.025	0.936	0.943	0.921	0.996	
	MSAM	1.006	0.047	0.054	0.020	0.026			MSAM	1.254	0.050	0.048	0.227	0.048	
	MPSNR	11.72	32.56	32.64	36.04	48.45			MPSNR	7.67	30.08	31.70	32.32	42.73	
0.8	MSSIM	0.359	0.974	0.966	0.977	0.998		0.1	MSSIM	0.081	0.952	0.958	0.957	0.996	
	MSAM	0.801	0.047	0.056	0.043	0.026			MSAM	1.141	0.049	0.061	0.085	0.048	
0.5	MPSNR	14.94	35.13	35.53	31.31	37.10		0.8	MPSNR	19.26	36.59	39.78	35.96	47.82	
	MSSIM	0.214	0.981	0.985	0.962	0.986			MSSIM	0.474	0.986	0.993	0.975	0.998	
	MSAM	0.826	0.047	0.047	0.135	0.044			MSAM	0.591	0.047	0.042	0.060	0.031	
	MPSNR	6.98	31.46	32.85	25.95	36.93			MPSNR	11.31	33.16	35.41	33.20	47.87	
	MSSIM	0.028	0.966	0.965	0.901	0.986			MSSIM	0.218	0.973	0.984	0.954	0.998	
	MSAM	1.197	0.049	0.060	0.284	0.044			MSAM	0.982	0.048	0.045	0.108	0.031	
	MPSNR	2.91	29.95	31.61	21.70	37.16			MPSNR	7.22	30.41	34.65	31.21	47.38	
	MSSIM	0.007	0.944	0.961	0.792	0.986			MSSIM	0.153	0.957	0.971	0.933	0.998	
	MSAM	1.329	0.050	0.063	0.467	0.050			MSAM	1.154	0.049	0.056	0.188	0.031	
	MPSNR	5.68	30.63	32.43	25.34	39.40			MPSNR	9.87	30.91	34.51	33.33	46.07	
0.1	MSSIM	0.028	0.948	0.964	0.894	0.989		0.1	MSSIM	0.239	0.965	0.972	0.961	0.996	
	MSAM	1.227	0.049	0.061	0.303	0.046			MSAM	0.992	0.048	0.057	0.073	0.034	

and mean spectral angle mapper (MSAM) [46], are used in our simulated experiments

$$\text{MPSNR} = \frac{1}{B} \sum_{i=1}^B \text{PSNR}_i$$

$$\text{MSSIM} = \frac{1}{B} \sum_{i=1}^B \text{SSIM}_i$$

$$\text{MSAM} = \frac{1}{MN} \sum_{i=1}^{MN} \arccos \frac{(\mathcal{X}^i)^T \cdot (\hat{\mathcal{X}}^i)}{\|\mathcal{X}^i\| \cdot \|\hat{\mathcal{X}}^i\|},$$

where PSNR_i and SSIM_i are the PSNR and SSIM values for the i th band, respectively. \mathcal{X}^i and $\hat{\mathcal{X}}^i$ are the i th spectral signatures of the ground-truth and desriping MSI, respectively. Especially, the MSAM is used to measure a global performance of spectral

distortion. The large values of MPSNR and MSSIM, and smaller MSAM indicate the better desriping results. Tables I and II display the desriping results by the four compared methods in terms of the all simulated periodic and nonperiodic stripes under different noise levels, respectively. The highest MPSNR and MSSIM, and smallest MSAM values are labeled in bold. From these two tables, we can see that the proposed LRTD method achieves the highest MPSNR and MSSIM and the significant improvement over the compared methods in all cases. Moreover, we can observe that the compared methods are not robust. As seen, the MPSNR and MSSIM values of the three compared methods are evidently decreased with the intensity of stripes increase, but the proposed method also obtains stable results. For the MSAM index, the proposed method achieves the smallest values in most cases when compared to the other methods, which verifies that our method generates the lowest spectral distortion.

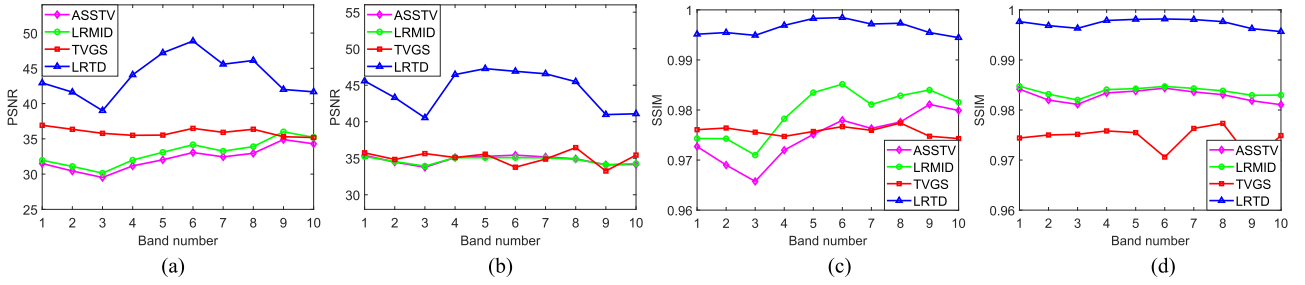


Fig. 6. PSNR and SSIM values of each band in case ($r = 0.5$ and $I = 0.2$). (a) PSNR values of periodic stripes. (b) PSNR values of nonperiodic stripes. (c) SSIM values of periodic stripes. (d) SSIM values of nonperiodic stripes.

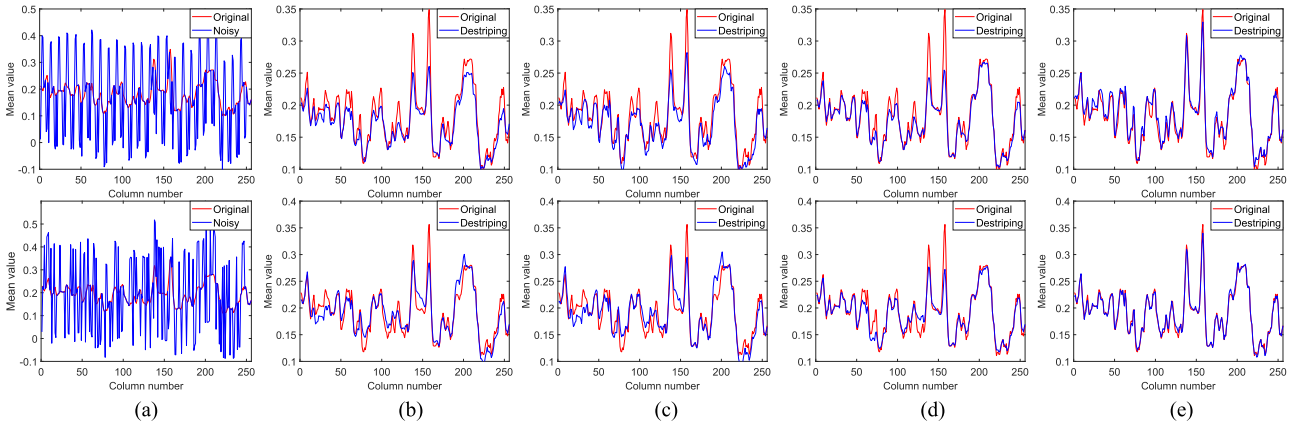


Fig. 7. Mean cross-track profiles for image shown in Fig. 2 (top row) and Fig. 4 (bottom row). (a) Striped. (b) ASSTV. (c) LRMID. (d) TVGS. (e) LRTD.

In summary, the quantitative comparison is in accordance with the above-mentioned visual results.

We further show the PSNR and SSIM values in each band for cases of Figs. 2 and 4. As the display in Fig. 6, we can observe that the PSNR and SSIM values of the proposed method are significantly higher than those of the compared methods in all bands, indicating that the proposed method indeed outperforms other methods for stripe noise removal. The similar observation also can be seen in other cases.

Qualitative comparison: Furthermore, we use the mean cross-track profile as the qualitative index to compare the performance of the all destriping methods. Fig. 7 shows the mean cross-track profiles of Figs. 2 and 4. The horizontal axis is the column number, and the vertical axis is the mean value of each column. Fig. 7(a) shows that there are rapid fluctuations in the curve (blue curve) due to the effects of the stripe noise. After destriping by the four methods, the fluctuations are strongly reduced as shown in Fig. 7(b)–(e). However, we can find that ASSTV, LRMID, and TVGS fail to restore original mean cross-track profile (red curve), which indicates that the destriping images may be distorted, blurred, and oversmoothed. This is in accordance with the visual results shown in Figs. 2–5. On the contrary, in Fig. 7(e), it can be observed that the mean cross-track profile of LRTD holds the same curve tendency as the original image. Moreover, to show the ability of estimating the stripe component, we also display the mean cross-track profile for the estimated stripe component. We also use Figs. 2 and 4 as the examples, and the estimated stripe component of ASSTV is the difference

of the degraded image with the destriping image. As shown in Fig. 8(a) and (b), ASSTV and LRMID fail to estimate the original stripe component and introduce some minor errors in stripe-free regions. TVGS obtains acceptable results compared with ASSTV and LRMID. In Fig. 8(d), it can be seen that the proposed method extracts the correct stripe component and does not introduce extra stripe error in stripe-free locations. Thus, in addition to removing the periodic and nonperiodic stripes effectively, our LRTD method also has a better ability to preserve the stripe-free information and detail.

2) Locations of Stripes are Identically Distributed in Each Band

In the above-mentioned experiments, we consider that the locations of stripes are randomly distributed in each band. In the following, we conduct a special stripe noise degradation, i.e., the location and intensity of stripes are identically distributed in each band. This situation is more difficult to track because the prior of the spectral dimension is completely dropped. Moreover, the information on the stripe locations fails to complement each other in all bands. To show the proposed method can track this problem, we similarly select the Washington DC Mall dataset as our second simulated experiments. The stripe noise generation is the same as mentioned above, but the location and degradation degree of the different band are identical. As the above-mentioned experiments have shown that our LRTD method has a better destriping performances in different stripe degradation levels, we only consider the percentage $r = 0.5$ and intensity $I = \{0.5, 0 - 1\}$ in this type of stripes.

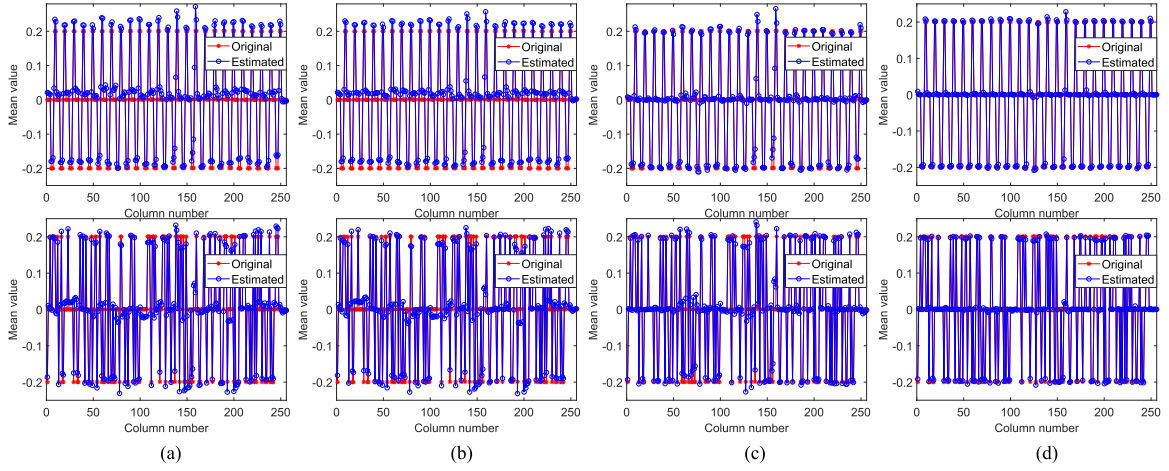


Fig. 8. Mean cross-track profiles for estimated stripes shown in Fig. 2 (top row) and Fig. 4 (bottom row). (a) ASSTV. (b) LRMID. (c) TVGS. (d) LRTD.

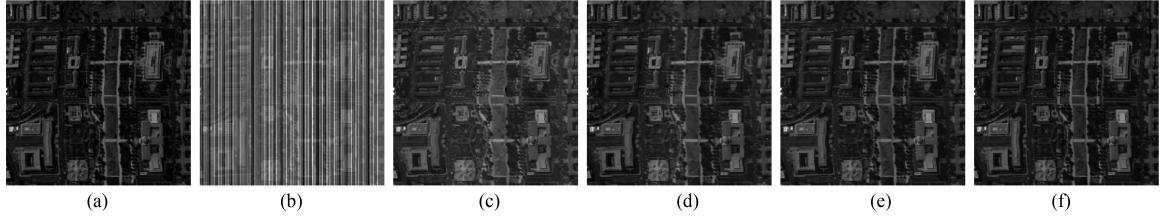


Fig. 9. Destriping results of band 10 for the periodic stripes case ($r = 0.5$ and $I = 0 - 1$). (a) Original. (b) Degraded image with periodic stripes. Destriping results of, (c) ASSTV, (d) LRMID, (e) TVGS, (f) LRTD.

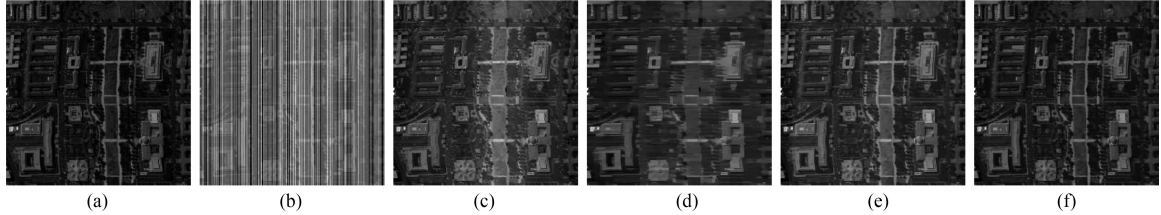


Fig. 10. Destriping results of band 5 for the nonperiodic stripes case ($r = 0.5$ and $I = 0 - 1$). (a) Original. (b) Degraded image with nonperiodic stripes. Destriping results of, (c) ASSTV, (d) LRMID, (e) TVGS, (f) LRTD.

Figs. 9 and 10 show the destriping results for periodic and nonperiodic stripes in this type of noise, respectively. ASSTV and LRMID can remove the stripes, but they smooth the details seriously, as presented in Figs. 9–10(c) and Figs. 9–10(d), respectively. TVGS can moderately preserve the details, but some stripe-like artifacts exist in the image shown in Fig. 9(e). Fig. 10(e) also shows that TVGS seriously blurs the image. From Figs. 9–10(f) to see, the proposed LRTD achieves the best destriping results, removing all of the stripes while preserving most of the structures and details in the image.

In Table III, we calculate the quantitative indices to show the performance of the destriping results in different degradation levels. As shown in this table, the proposed method still obtains the highest values in terms of MPSNR and MSSIM, which again indicates that the proposed method can track this situation efficiently. TVGS gets the satisfactory results because it handles the stripes band by band. The visual comparison shows that the

stripes are completely removed by ASSTV and LRMID. To show the difference between the compared methods, we show the qualitative comparison. Fig. 11 shows the mean cross-track profile of the destriping image. It is easy to observe that the restored curves of ASSTV, LRMID, and TVGS deviate from the original curve, which illustrates image distortion and blur in the image. The results of the proposed method, which are shown in Fig. 11(e), are more reasonable, indicating that the proposed method can track this type of stripes.

B. Real Data Experiments

To illustrate the robustness of the proposed method, we also choose four real image in our real data experiments. Since in some real MSI imaging scenarios, the MSI is not only contaminated by stripe noise, but also degraded by some random noises, thus two of the four data are degraded by the stripe noise

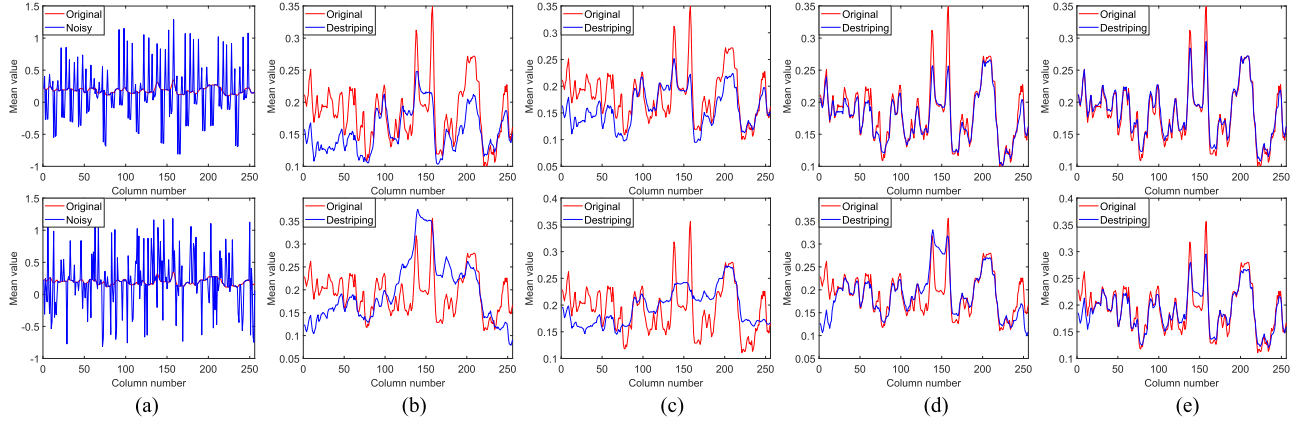


Fig. 11. Mean cross-track profiles for image shown in Fig. 9 (top row) and Fig. 10 (bottom row). (a) Striped. (b) ASSTV. (c) LRMID. (d) TVGS. (e) LRTD.

TABLE III
QUANTITATIVE EVALUATION OF THE DIFFERENT METHODS FOR THE STRIPES
UNDER DIFFERENT NOISE LEVELS ON WASHINGTON DC MALL

Periodic stripes							
r	I	Index	Degrade	ASSTV	LRMID	TVGS	LRTD
0.5	MPSNR	9.13	25.25	25.7	34.19	38.85	
	MSSIM	0.053	0.869	0.898	0.964	0.988	
	MSAM	0.899	0.119	0.054	0.009	0.037	
	MPSNR	8.28	25.73	26.67	34.05	38.85	
0-1	MSSIM	0.079	0.893	0.913	0.963	0.989	
	MSAM	0.749	0.053	0.066	0.009	0.036	
Nonperiodic stripes							
r	I	Index	Degrade	ASSTV	LRMID	TVGS	LRTD
0.5	MPSNR	9.03	23.58	24.57	26.64	33.90	
	MSSIM	0.078	0.874	0.721	0.928	0.973	
	MSAM	0.768	0.091	0.072	0.074	0.048	
	MPSNR	8.10	22.99	24.41	28.18	34.46	
0-1	MSSIM	0.084	0.871	0.721	0.943	0.974	
	MSAM	0.573	0.076	0.043	0.037	0.048	

with random noise. The first data is the Hyperion image, which was also used in [32], and the subimage of $256 \times 256 \times 10$ is extracted for our experiment. The HYDICE Urban data is employed as the second data. The original size of the image is $307 \times 307 \times 210$, and some of the bands are contaminated by nonperiodic stripes. We extract a subimage of $307 \times 307 \times 8$ as our experimental data. The third real data adopt an EO-1 Hyperion image as the test image, which is mainly corrupted by stripes and random noise. The original image size is $3631 \times 256 \times 198$, and a subimage of size $254 \times 254 \times 10$ is used in our experiment. The last one CHRIS is a push-broom scanner with the ability to obtain images from five different angles [15]. In our study, we choose an image obtained using mode-2, which has 748×766 pixels with 18 bands. The image was collected on October 18, 2005. A subimage of $698 \times 698 \times 10$ of this image is adopted to test the experiment.

Figs. 12–15 show the destriping results of the different methods for the four real datasets. From Figs. 12–13(a), we can see that the Hyperion data and Urban data are degraded by the nonperiodic stripes. Figs. 14–15(a) show that the EO-1 Hyperion data and CHRIS data are seriously contaminated by the

stripe noise and tiny random noise. From the results, we have the following observations. First, ASSTV, LRMID, and TVGS can efficiently remove the stripe noise when the image is only degraded by the stripe noise (see Figs. 12–13). Second, when the image is degraded by the mixture noise, ASSTV only can remove the stripe noise, but the random noise is also left in the image as shown in Figs. 14–15(b). LRMID can eliminate the most of the mixture noise, but the image details and texture are destroyed as shown in Figs. 14–15(c). As shown in Figs. 14–15(d), TVGS fails to remove the obvious stripe and the random noise. Third, no matter how degraded the image is, the proposed method can effectively remove the noise as well as preserving the image details. For convenience of comparison, the detailed regions extracted from Fig. 15 are presented in Fig. 16. It can be easily observed that LRMID and the proposed method obtain more smoothness results, and with ASSTV, the random noise exists in the image. In summary, the proposed LRTD method can simultaneously remove the stripe noise and random noise, and effectively preserve the details, which indicates that the proposed method is more practical in real MSI destriping compared with other three methods.

For the quantitative assessment in the real data experiments, since without the ground-truth image as reference data, we use two nonreference indices, the inverse coefficient of variation (ICV) [16], [21], [32] and mean relative deviation (MRD) [16], [21], [32], to evaluate the destriping results. The indices ICV and MRD are specific for evaluating the destriping performance. ICV evaluates the level of stripe noise and so would be calculated for homogeneous striped regions. Conversely, the MRD index is employed to evaluate the performance of the methods to preserve the information of nonstriped regions. These indices are defined as follows [16], [21]:

$$\text{ICV} = \frac{R_m}{R_s},$$

$$\text{MRD} = \frac{1}{MN} \sum_i \frac{|x_i - y_i|}{y_i} \times 100\%$$

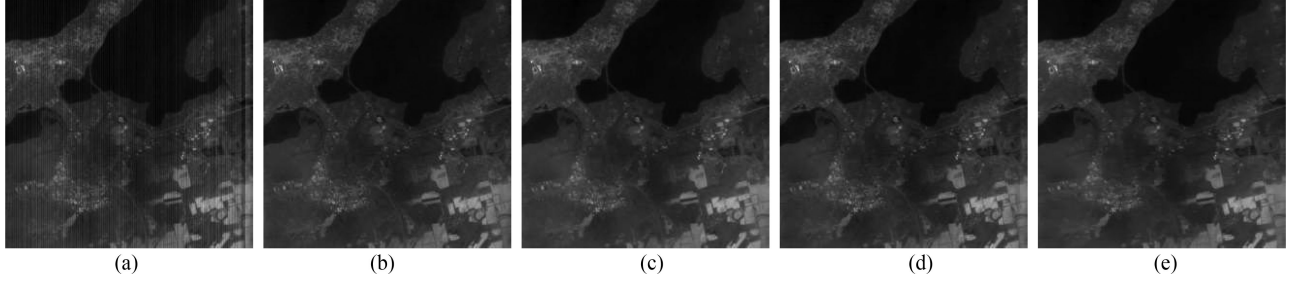


Fig. 12. Destriping results of band 3 in real data 1. (a) Original. Destriping results by, (b) ASSTV, (c) LRMID, (d) TVGS, (e) LRTD.



Fig. 13. Destriping results of band 8 in real data 2. (a) Original. Destriping results by, (b) ASSTV, (c) LRMID, (d) TVGS, (e) LRTD.

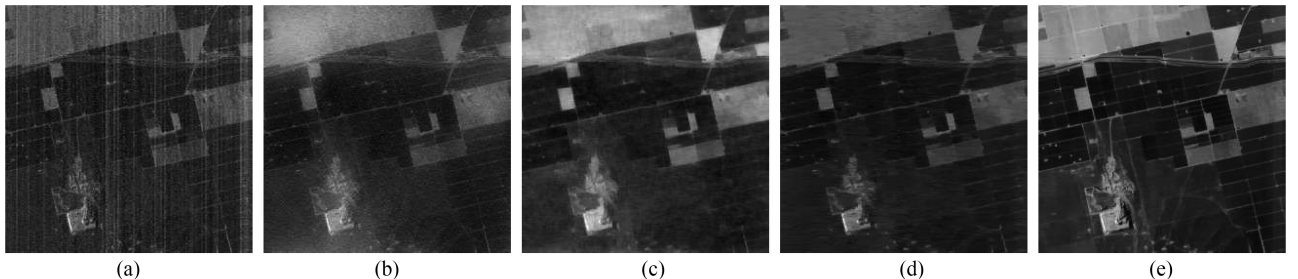


Fig. 14. Destriping results of band 1 in real data 3. (a) Original. Destriping results by, (b) ASSTV, (c) LRMID, (d) TVGS, (e) LRTD.

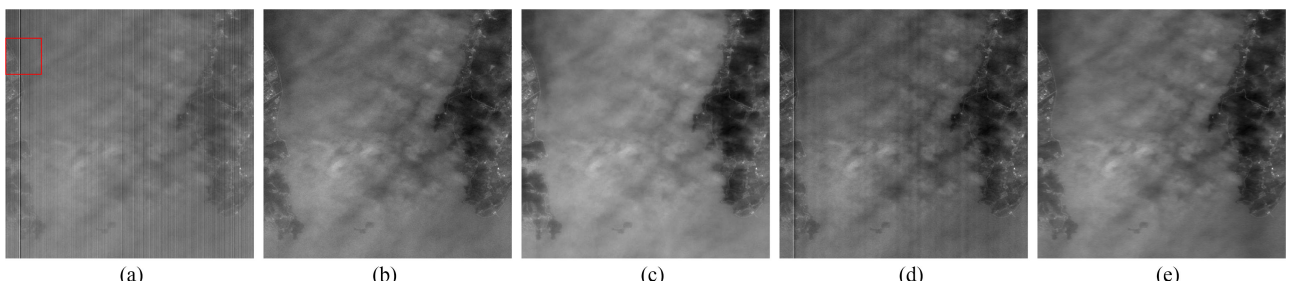


Fig. 15. Destriping results of band 1 in real data 4. (a) Original. Destriping results by, (b) ASSTV, (c) LRMID, (d) TVGS, (e) LRTD.

where R_m and R_s are the mean and standard deviation of pixel values, respectively. x_i and y_i are the pixel values in the destriping and striped images, respectively.

In our experiments, we select the homogenous regions with a window of 10×10 pixels to calculate the ICV and MRD indices in each band, and then the mean value of these indices for the whole MSI is calculated and denoted as MICV and MMRD. Moreover, we separately select three sampled homogenous re-

gions and sharp nonstripe regions to calculate the indices MICV and MMRD. It is worthy to point out that since there is an absence of 10×10 nonstripe region in Figs. 12, 14, and 15, we only calculate the MMRD in Urban data. In general, higher MICV and lower MMRD indicate the better destriping results. The better MICV and MMRD values are labeled in bold in each sample. The visual comparison of Figs. 12 and 13 show that the results of different methods are the same. However,

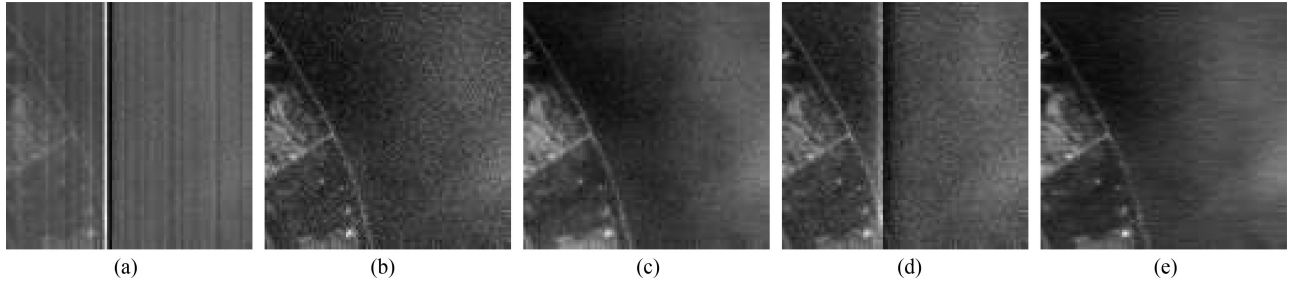


Fig. 16. Magnified results of Fig. 15. (a) Original. Desstriping results by, (b) ASSTV, (c) LRMID, (d) TVGS, (e) LRTD.

TABLE IV
QUANTITATIVE EVALUATION OF DIFFERENT METHODS FOR THE REAL DATA EXPERIMENTS

Image	Index	Noisy	ASSTV	LRMID	TVGS	LRTD
data 1	MICV1	66.54	160.56	190.60	190.18	250.47
	MICV2	33.07	51.20	52.62	49.85	54.41
	MICV3	33.28	54.21	63.00	55.57	70.04
data 2	MICV1	13.07	13.81	15.51	14.07	16.03
	MICV2	15.22	16.61	20.63	16.78	19.09
	MICV3	16.57	18.66	19.46	19.03	21.16
	MMRD1	-	0.034	0.032	0.020	0.029
	MMRD2	-	0.048	0.070	0.019	0.040
	MMRD3	-	0.045	0.045	0.021	0.039
data 3	MICV1	4.01	5.65	7.98	8.31	11.60
	MICV2	6.81	10.22	15.22	15.99	19.86
	MICV3	4.13	5.88	7.97	13.91	20.09
data 4	MICV1	86.09	79.85	101.02	103.88	115.02
	MICV2	27.36	187.89	336.58	256.44	344.41
	MICV3	44.42	90.40	100.37	95.77	101.51

as displayed in the nonreference indices MICV and MMRD in Table IV, the proposed LRTD obtains the higher MICV except one sample, which indicates that the desstriping ability of the proposed method outperforms the compared methods. For the MMRD index in Urban data, TVGS performs the lower values; the reason is that it implements the desstriping band by band. Compared with the MSI desstriping methods ASSTV and LRMID, the proposed method achieves the lower MMRD values. Thus the proposed method has the better ability for preserving the information of the nonstripe regions than ASSTV and LRMID.

C. Discussion

In this discussion, we will analyze the sensitivity of the parameters involved in the proposed LRTD method. There are seven parameters that should be determined before performing the Algorithm 1 for MSI desstriping, including three regularization parameters λ_1 , λ_2 , and λ_3 , the positive penalty parameter β , and three estimated rank parameters $[r_1, r_2, r_3]$ along the three modes in Tucker decomposition for stripe component. To show the practicability of our LRTD method, we only fine tune the three regularization parameters in all our experiments, which simplifies the numbers of the parameter adjustment. For the positive penalty parameter β , we set $\beta = 0.1$. r_1 and r_2 depict the complexity of spatial redundancy, and r_3 depicts the complexity

of temporal redundancy. In our study, we suppose that the pixel values of each stripe line are identical, and the stripe locations of each band are random distribution. Thus for the estimated rank parameters $[r_1, r_2, r_3]$, we approximately set it as $[1, B, B]$. It is worth noting that this assumption may be violated in some data, but the other regularization terms can help to remove the stripes even though the Tucker decomposition fails to precisely estimate the stripe component.

In the following, we need to present how to determine the three regularization parameters λ_1 , λ_2 , and λ_3 . Since the specific noise levels and percentages of stripes vary a lot in our experiments, thus the corresponding regularization parameters in our model need to be fine tuned according to the different degradation levels of the test image. To clearly show the sensitivity analyses of the regularization parameters, we select four different stripe degradation levels from the simulated data experiments as the examples, i.e., periodic stripes and nonperiodic stripes in the case of $r = 0.2$, $I = 0.2$ and $r = 0.8$, $I = 0.8$, respectively. We use the MPSNR index as the evaluation measure to evaluate the selection of these parameters.

1) *Sensitivity Analysis of Parameter λ_1 :* In the LRTD solver, λ_1 is used to balance the smoothness of the desired image in the spatial horizontal direction, which depends on the stripe level. Fig. 17 shows the curves of the MPSNR values with the change of the parameter λ_1 in different degradation levels. In Fig. 17(a) and (c), we can observe that MPSNR achieves the optimal performance when λ_1 that is chosen, is near to 0.0005. However, from Fig. 17(b) and (d), we can see that the proposed method performs best when $\lambda_1 = 0.001$ and $\lambda_1 = 0.005$, respectively. We set $r = 0.2$, $I = 0.2$ as the sparse stripes case and $r = 0.8$, $I = 0.8$ as dense stripes. Therefore, we can summarize a conclusion for the selection of parameter λ_1 . When the stripes are sparse in the image, we should select a smaller λ_1 value. On the contrary, a higher λ_1 would more suitable for the dense stripe situation. Since the different degradation levels of the stripe noise in our experiments, we empirically set λ_1 varied in the set of $\{0.0005, 0.001, 0.005\}$.

2) *Sensitivity Analysis of Parameter λ_2 :* In the LRTD solver, λ_2 is used to control the spectral consistency. For MSI, the spectral consistency is a very important prior, which can help us to suppress the stripe noise and preserve the spectral information, especially for the locations of the stripe noise whose distribution is different on adjacent bands. Fig. 18 presents the MPSNR values of the LRTD solver with different λ_2 values in four

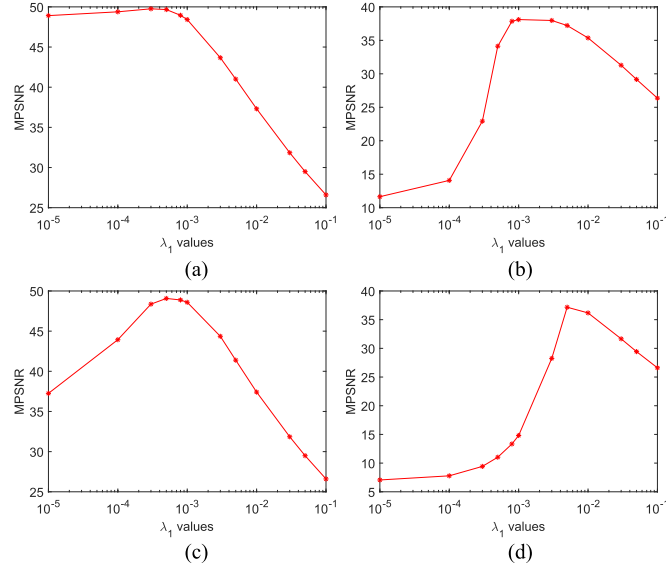


Fig. 17. Sensitivity analysis of parameter λ_1 in four different stripe degradation levels. (a) Periodic stripes ($r = 0.2, I = 0.2$). (b) Periodic stripes ($r = 0.8, I = 0.8$). (c) Nonperiodic stripes ($r = 0.2, I = 0.2$). (d) Nonperiodic stripes ($r = 0.8, I = 0.8$).

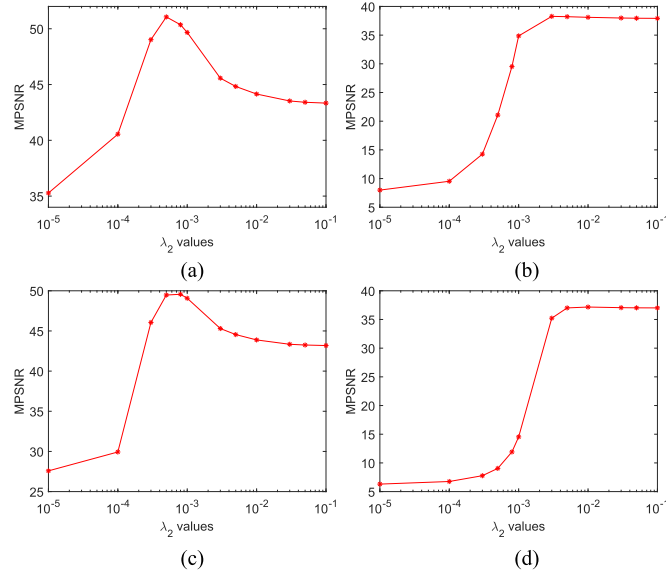


Fig. 18. Sensitivity analysis of parameter λ_2 in four different stripe degradation levels. (a) Periodic stripes ($r = 0.2, I = 0.2$). (b) Periodic stripes ($r = 0.8, I = 0.8$). (c) Nonperiodic stripes ($r = 0.2, I = 0.2$). (d) Nonperiodic stripes ($r = 0.8, I = 0.8$).

different degradation levels. From the figures to see, it can be observed that the smaller λ_2 value also applies to sparse stripes, and dense stripes should select a higher value. Thereby, we set $\lambda_2 = 0.001$ when the stripe noise is sparse in the image, and for dense stripes, we set $\lambda_2 = 0.01$. In all our experiments, we empirically set λ_2 varied in the set of $\{0.001, 0.005, 0.01\}$.

3) Sensitivity Analysis of Parameter λ_3 : Fig. 19 plots the experimental results of MPSNR versus the parameter λ_3 under different of the degradation levels. It can be observed that these regularization terms can improve the experimental results even

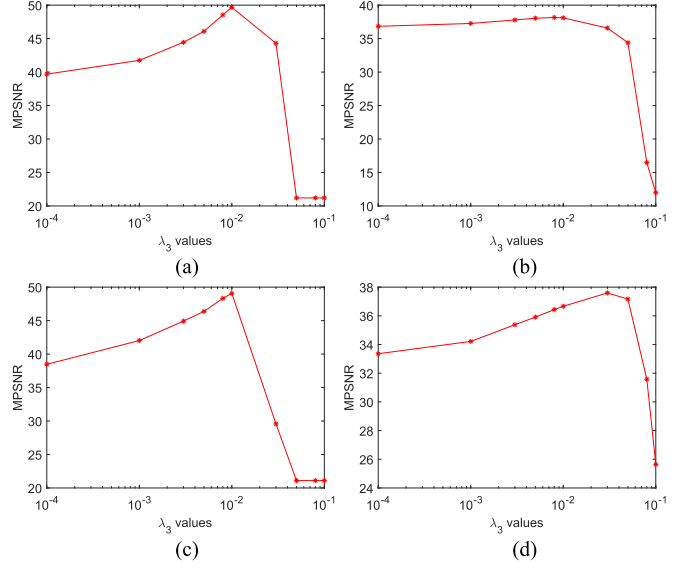


Fig. 19. Sensitivity analysis of parameter λ_3 in four different stripe degradation levels. (a) Periodic stripes ($r = 0.2, I = 0.2$). (b) Periodic stripes ($r = 0.8, I = 0.8$). (c) Nonperiodic stripes ($r = 0.2, I = 0.2$). (d) Nonperiodic stripes ($r = 0.8, I = 0.8$).

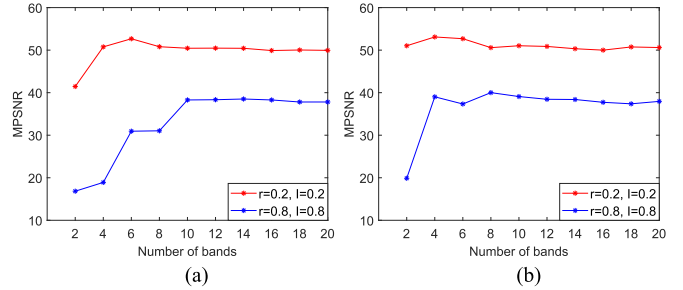


Fig. 20. Sensitivity analysis of the number of bands in four different stripe degradation levels. (a) Periodic stripes. (b) Nonperiodic stripes.

though the stripe component violates the group sparsity prior when the stripes are dense in the image. From Fig. 19(a)–(c) to see, the highest MPSNR values are achieved due to the optimal performance with $\lambda_3 = 0.01$. However, Fig. 19(d) shows that the destriping result is obtained best when $\lambda_3 = 0.05$. Therefore, for the selection of parameter λ_3 , our recommended set of candidate values is $\{0.01, 0.05\}$.

Overall, the parameter setting of our proposed LRTD method is relatively stable, because the alternative values of the parameters λ_1 , λ_2 , and λ_3 are only a few. Moreover, the penalty parameter β and estimated rank parameters $[r_1, r_2, r_3]$ do not need to be manually adjusted. In the following, we will analyze the effects of the number of bands in our MSI destriping and the spectral analysis. Finally, we will present the numerical convergence of our proposed method.

4) Effects of the Number of Bands: In our simulated experiments, the number of bands is chosen as 10. In general, the large number of bands may improve the destriping results because the more information can complement each band. However, it can result in the obvious increase of the computational cost. Fig. 20 shows the changes of the MPSNR values with the different num-

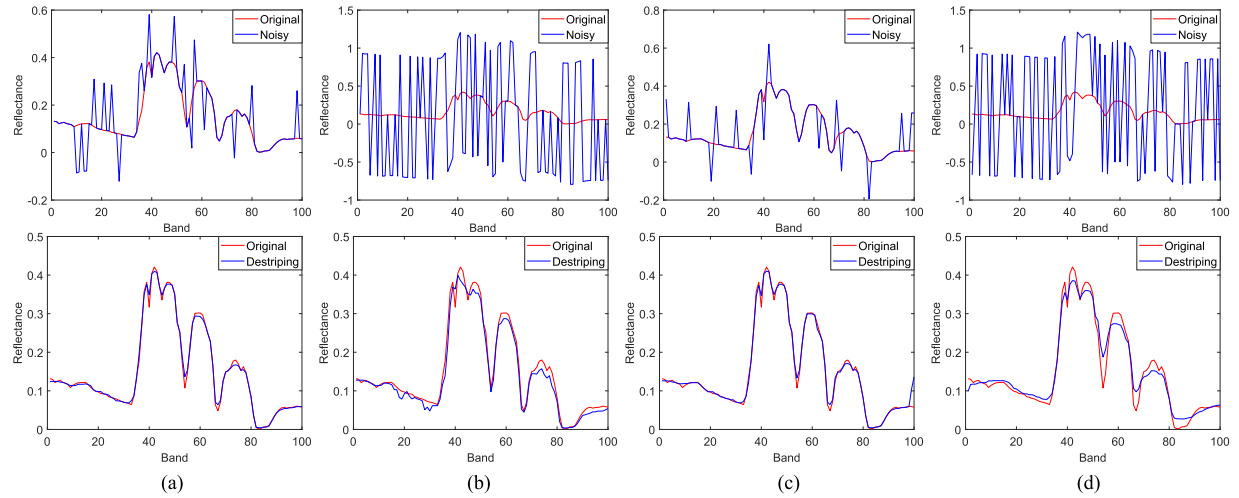


Fig. 21. Spectrum of pixel (200, 250) in the destriping results. (a) Periodic stripes ($r = 0.2, I = 0.2$). (b) Periodic stripes ($r = 0.8, I = 0.8$). (c) Nonperiodic stripes ($r = 0.2, I = 0.2$). (d) Nonperiodic stripes ($r = 0.8, I = 0.8$).

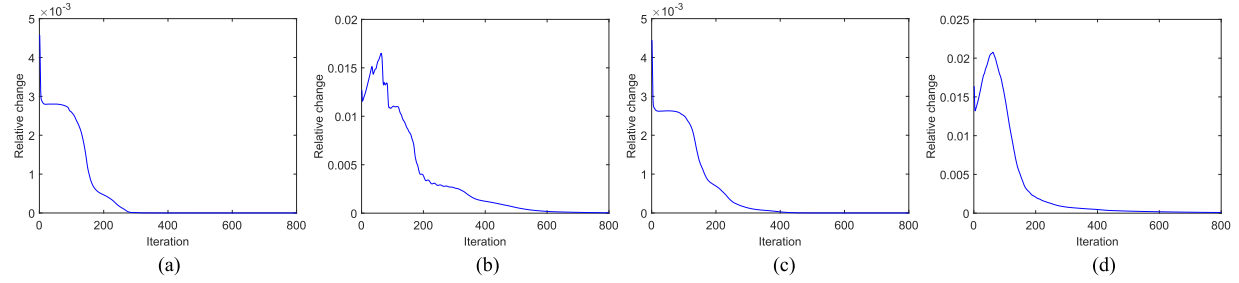


Fig. 22. Relative change $\frac{\|\mathcal{X}^{k+1} - \mathcal{X}^k\|_F}{\|\mathcal{X}^k\|_F}$ values versus the iteration number of the LRTD solver in four different stripe degradation levels. (a) Periodic stripes ($r = 0.2, I = 0.2$). (b) Periodic stripes ($r = 0.8, I = 0.8$). (c) Nonperiodic stripes ($r = 0.2, I = 0.2$). (d) Nonperiodic stripes ($r = 0.8, I = 0.8$).

ber of bands in four different degradation levels. From Fig. 20(a) and the blue curve in Fig. 20(b), it can be observed that the MPSNR values achieved gradually increase when the number of bands is increased. Nevertheless, the MPSNR values tend to remain stable when the number of bands is large than 10. Thereby, we set the number of bands as 10 in our simulated experiments.

5) *Spectral Analysis*: In this part, we further show that the proposed LRTD method can efficiently preserve the important spectral information before and after restoration. To clearly illustrate the performance, we select a subimage of 256×256 pixels with 100 spectral bands from the Washington DC Mall to add four different stripe levels and then show the spectral signatures. Fig. 21 shows the spectral signatures of pixel (200, 250) in different stripe cases. From the top of Fig. 21 to see, there are many impulses in the curves due to the effects of the stripe noise. After destriping, the impulses are all reduced as shown in the bottom of Fig. 21. In Fig. 21(a)–(c), the spectral information of all bands is well preserved because the curves of our results are basically the same as the original curves. Although the spectral information deviates original signatures in some bands as shown in Fig. 21(d), most of the spectral information is also greatly maintained. In general, the result of Fig. 21 is sufficient to indicate that our method can effectively preserve the spectral signatures in different stripe cases.

6) *Numerical convergence of the LRTD solver*: It is easy to see that our LRTD model (6) is a nonconvex optimization problem because of the nonconvexity of Tucker decomposition. For a nonconvex problem, it is hard to find a globally optimal solution and prove the convergence of the algorithm. In our study, we introduce an efficient ALM method to optimize our LRTD model. To show the empirical analysis for the convergence of our LRTD solver, we present the evolutional curve of the relative change $\frac{\|\mathcal{X}^{k+1} - \mathcal{X}^k\|_F}{\|\mathcal{X}^k\|_F}$ values versus the iteration number in four different experimental cases. From the curves of the relative change presented in Fig. 22, we can observe that though there is a significant jump of the relative change in some cases, the relative change converges to zero when the algorithms reach a relatively high iteration number, indicating that the convergence of the LRTD solver can be numerically guaranteed.

7) *Running time*: To measure the efficiency of the proposed method, we show that the running time of four compared methods on four real data experiments in Table V. From the table to see, the proposed method obtains the acceptable running time compared with other methods. The reason is that the proposed method needs to iterate hundreds of times to achieve the convergence shown in Fig. 22; as a result, the running time is not the fastest. In the future, we will design a more effective algorithm

TABLE V
RUNNING TIME (IN SECONDS) OF THE DIFFERENT METHODS IN THE REAL DATA EXPERIMENTS

Data	ASSTV	LRMID	TVGS	LRTD
data 1	14.48	48.53	9.19	18.93
data 2	26.11	65.82	18.97	18.47
data 3	19.09	54.37	16.45	35.49
data 4	154.46	416.87	655.12	506.47

to speed up our method. Although our method is not the fastest, we perform better than others mentioned above.

V. CONCLUSION

In this paper, we proposed a novel LRTD framework for MSI despeckling. Different from the existing despeckling methods, the image component and stripe component are both modeled as tensor-based representation in our work. The spatial unidirectional TV and spectral TV regularization on the image can enhance the piecewise smoothness of the image component without the stripe component, whereas the low-rank tensor Tucker decomposition and $\ell_{2,1}$ -norm regularization are utilized to depict the global spatial correlation and group sparsity characteristic of the stripe component among all bands, which can discriminatively distinguish the stripe component from the image component. To effectively solve the nonconvex tensor optimization model, we design a popular algorithm based on the ALM method. Compared with existing despeckling methods, the proposed method has achieved the better despeckling performance tested on various simulated stripe cases and real striped image.

Despite the proposed LRTD achieves a good performance for horizontal or vertical stripes, it fails to handle the oblique stripes in georeferenced images. In the future, the rotation strategy [47], [48] can be incorporated into our LRTD model to track the oblique stripes. Moreover, we will try to extend the application of our method to video rain streak removal by incorporating rotation strategy. Finally, the deep learning ideas of infrared image stripe noise removal [49] can be extended to remote sensing image despeckling.

ACKNOWLEDGMENT

The authors would like to thank the Editors and the anonymous reviewers for their constructive comments which helped to improve the quality of the paper. The authors would like to thank Dr. Yi Chang for providing the free download of the source code for ASSTV and LRMID and sharing the Hyperion dataset, and Dr. Biao Cao for sharing the CHRIS dataset.

REFERENCES

- [1] J. Chen, Y. Shao, H. Guo, W. Wang, and B. Zhu, "Despeckling CMODIS data by power filtering," *IEEE Trans. Geosci. Remote Sens.*, vol. 41, no. 9, pp. 2119–2124, Sep. 2003.
- [2] N. Yokoya, X. X. Zhu, and A. Plaza, "Multisensor coupled spectral unmixing for time-series analysis," *IEEE Trans. Geosci. Remote Sens.*, vol. 55, no. 5, pp. 2842–2857, May 2017.
- [3] N. Yokoya, C. Grohnfeldt, and J. Chanussot, "Hyperspectral and multispectral data fusion: A comparative review of the recent literature," *IEEE Geosci. Remote Sens. Mag.*, vol. 5, no. 2, pp. 29–56, Jun. 2017.
- [4] Q. Liu, L. Liu, and Y. Wang, "Unsupervised change detection for multispectral remote sensing images using random walks," *Remote Sens.*, vol. 9, no. 5, p. 438, 2017.
- [5] S. K. Sinha and L. K. Tiwari, "Enhancement of image classification for forest encroachment mapping with destriped SWIR band in the wavelet domain," *IEEE J. Sel. Topics Appl. Earth Observ. Remote Sens.*, vol. 11, no. 7, pp. 2276–2281, Jul. 2018.
- [6] J. Chen and C. Chang, "Destriping of landsat MSS images by filtering techniques," *Photogrammetric Eng. Remote Sens.*, vol. 58, no. 10, pp. 1417–1423, 1992.
- [7] J. Chen, H. Lin, Y. Shao, and L. Yang, "Oblique striping removal in remote sensing imagery based on wavelet transform," *Int. J. Remote Sens.*, vol. 27, no. 8, pp. 1717–1723, 2006.
- [8] J. Torres and S. O. Infante, "Wavelet analysis for the elimination of striping noise in satellite images," *Opt. Eng.*, vol. 40, no. 7, pp. 1309–1314, 2001.
- [9] B. M. Rnch, P. Trtik, F. Marone, and M. Stampanoni, "Stripe and ring artifact removal with combined wavelet—Fourier filtering," *Opt. Express*, vol. 17, no. 10, pp. 8567–8591, 2009.
- [10] R. Pande-Chhetri and A. Abd-Elrahman, "De-striping hyperspectral imagery using wavelet transform and adaptive frequency domain filtering," *ISPRS J. Photogrammetric Remote Sens.*, vol. 66, no. 5, pp. 620–636, 2011.
- [11] L. Sun, R. Neville, K. Staenz, and H. P. White, "Automatic despeckling of hyperion imagery based on spectral moment matching," *Can. J. Remote Sens.*, vol. 34, no. S1, pp. S68–S81, 2008.
- [12] F. Gadallah, F. Csillag, and E. Smith, "Despeckling multisensor imagery with moment matching," *Int. J. Remote Sens.*, vol. 21, no. 12, pp. 2505–2511, 2000.
- [13] M. Wegener, "Despeckling multiple sensor imagery by improved histogram matching," *Int. J. Remote Sens.*, vol. 11, no. 5, pp. 859–875, 1990.
- [14] P. Rakwatin, W. Takeuchi, and Y. Yasuoka, "Stripe noise reduction in MODIS data by combining histogram matching with facet filter," *IEEE Trans. Geosci. Remote Sens.*, vol. 45, no. 6, pp. 1844–1856, Jun. 2007.
- [15] B. Cao, Y. Du, D. Xu, H. Li, and Q. Liu, "An improved histogram matching algorithm for the removal of striping noise in optical remote sensing imagery," *Optik*, vol. 126, no. 23, pp. 4723–4730, 2015.
- [16] H. Shen and L. Zhang, "A MAP-based algorithm for despeckling and inpainting of remotely sensed images," *IEEE Trans. Geosci. Remote Sens.*, vol. 47, no. 5, pp. 1492–1502, May 2009.
- [17] M. Bouali and S. Ladjal, "Toward optimal despeckling of MODIS data using a unidirectional variational model," *IEEE Trans. Geosci. Remote Sens.*, vol. 49, no. 8, pp. 2924–2935, Aug. 2011.
- [18] Y. Chang, H. Fang, L. Yan, and H. Liu, "Robust despeckling method with unidirectional total variation and framelet regularization," *Opt. Express*, vol. 21, no. 20, pp. 23 307–23 323, 2013.
- [19] Y. Chang, L. Yan, H. Fang, and H. Liu, "Simultaneous despeckling and denoising for remote sensing images with unidirectional total variation and sparse representation," *IEEE Geosci. Remote Sens. Lett.*, vol. 11, no. 6, pp. 1051–1055, Jun. 2014.
- [20] Y. Zhang, G. Zhou, L. Yan, and T. Zhang, "A despeckling algorithm based on TV-stokes and unidirectional total variation model," *Optik*, vol. 127, no. 1, pp. 428–439, 2016.
- [21] X. Liu, H. Shen, Q. Yuan, X. Lu, and C. Zhou, "A universal despeckling framework combining 1-D and 2-D variational optimization methods," *IEEE Trans. Geosci. Remote Sens.*, vol. 56, no. 2, pp. 808–822, Feb. 2018.
- [22] Y. Chen, T. Z. Huang, L. J. Deng, X. L. Zhao, and M. Wang, "Group sparsity based regularization model for remote sensing image stripe noise removal," *Neurocomput.*, vol. 267, no. 6, pp. 95–106, 2017.
- [23] H. Carfantan and J. Idier, "Statistical linear despeckling of satellite-based pushbroom-type images," *IEEE Trans. Geosci. Remote Sens.*, vol. 48, no. 4, pp. 1860–1871, Apr. 2010.
- [24] X. Liu, X. Lu, H. Shen, Q. Yuan, Y. Jiao, and L. Zhang, "Stripe noise separation and removal in remote sensing images by consideration of the global sparsity and local variational properties," *IEEE Trans. Geosci. Remote Sens.*, vol. 54, no. 5, pp. 3049–3060, May 2016.
- [25] N. Acito, M. Diani, and G. Corsini, "Subspace-based striping noise reduction in hyperspectral images," *IEEE Trans. Geosci. Remote Sens.*, vol. 49, no. 4, pp. 1325–1342, Apr. 2011.
- [26] Y. Chang, L. Yan, T. Wu, and S. Zhong, "Remote sensing image stripe noise removal: From image decomposition perspective," *IEEE Trans. Geosci. Remote Sens.*, vol. 54, no. 12, pp. 7018–7031, 2016.
- [27] Y. Chen, T. Z. Huang, X. L. Zhao, L. J. Deng, and J. Huang, "Stripe noise removal of remote sensing images by total variation regularization and group sparsity constraint," *Remote Sens.*, vol. 9, no. 6, p. 559, 2017.
- [28] Y. Chang, L. Yan, H. Fang, S. Zhong, and Z. Zhang, "Weighted low-rank tensor recovery for hyperspectral image restoration," 2017, arXiv:1709.00192.

- [29] W. He, H. Zhang, L. Zhang, and H. Shen, "Total-variation-regularized low-rank matrix factorization for hyperspectral image restoration," *IEEE Trans. Geosci. Remote Sens.*, vol. 54, no. 1, pp. 178–188, 2016.
- [30] Y. Chen, T.-Z. Huang, X.-L. Zhao, and L.-J. Deng, "Hyperspectral image restoration using framelet-regularized low-rank nonnegative matrix factorization," *Appl. Math. Model.*, vol. 63, pp. 128–147, 2018.
- [31] X. Lu, Y. Wang, and Y. Yuan, "Graph-regularized low-rank representation for destriping of hyperspectral images," *IEEE Trans. Geosci. Remote Sens.*, vol. 51, no. 7, pp. 4009–4018, Jul. 2013.
- [32] Y. Chang, L. Yan, H. Fang, and C. Luo, "Anisotropic spectral-spatial total variation model for multispectral remote sensing image destriping," *IEEE Trans. Image Process.*, vol. 24, no. 6, pp. 1852–1866, Jun. 2015.
- [33] W. Cao, Y. Chang, G. Han, and J. Li, "Destriping remote sensing image via low-rank approximation and nonlocal total variation," *IEEE Geosci. Remote Sens. Lett.*, vol. 15, no. 6, pp. 848–852, Jun. 2018.
- [34] D. Cerra, R. Miller, and P. Reinartz, "Unmixing-based denoising for destriping and inpainting of hyperspectral images," in *Proc. IEEE Geosci. Remote Sens. Symp.*, 2014, pp. 4620–4623.
- [35] W. Cao et al., "Total variation regularized tensor RPCA for background subtraction from compressive measurements," *IEEE Trans. Image Process.*, vol. 25, no. 9, pp. 4075–4090, Sep. 2016.
- [36] Y. Wang, J. Peng, Q. Zhao, Y. Leung, X. L. Zhao, and D. Meng, "Hyperspectral image restoration via total variation regularized low-rank tensor decomposition," *IEEE J. Sel. Topics Appl. Earth Observ. Remote Sens.*, vol. 11, no. 4, pp. 1227–1243, Apr. 2018.
- [37] T. G. Kolda and B. W. Bader, "Tensor decompositions and applications," *SIAM Rev.*, vol. 51, no. 3, pp. 455–500, 2009.
- [38] X. L. Zhao, W. Wang, T. Y. Zeng, T. Z. Huang, and M. K. Ng, "Total variation structured total least squares method for image restoration," *SIAM J. Sci. Comput.*, vol. 35, no. 6, pp. B1304–B1320, 2013.
- [39] X. L. Zhao, F. Wang, and M. K. Ng, "A new convex optimization model for multiplicative noise and blur removal," *SIAM J. Imag. Sci.*, vol. 7, no. 1, pp. 456–475, 2014.
- [40] J. J. Mei, Y. Dong, T. Z. Huang, and W. Yin, "Cauchy noise removal by nonconvex ADMM with convergence guarantees," *J. Sci. Comput.*, vol. 74, no. 2, pp. 1–24, 2018.
- [41] Z. Lin, M. Chen, and Y. Ma, "The augmented lagrange multiplier method for exact recovery of corrupted low-rank matrices," 2010, arXiv:1009.5055.
- [42] D. L. Donoho, "De-noising by soft-thresholding," *IEEE Trans. Inf. Theory*, vol. 41, no. 3, pp. 613–627, May 1995.
- [43] G. Liu, Z. Lin, S. Yan, J. Sun, Y. Yu, and Y. Ma, "Robust recovery of subspace structures by low-rank representation," *IEEE Trans. Pattern Anal. Mach. Intell.*, vol. 35, no. 1, pp. 171–184, Jan. 2013.
- [44] M. Ishteva, L. De Lathauwer, P. A. Absil, and S. Van Huffel, "Differential-geometric newton method for the best rank-(r1, r2, r3) approximation of tensors," *Numer. Algorithms*, vol. 51, no. 2, pp. 179–194, 2009.
- [45] Z. Wang, A. C. Bovik, H. R. Sheikh, and E. P. Simoncelli, "Image quality assessment: From error visibility to structural similarity," *IEEE Trans. Image Process.*, vol. 13, no. 4, pp. 600–612, Apr. 2004.
- [46] R. Yuhas, A. F. H. Goetz, and J. W. Boardman, "Discrimination among semi-arid landscape endmembers using the spectral angle mapper (SAM) algorithm," in *Proc. Summaries 4th JPL Airborne Earth Sci. Workshop*, 1992, pp. 147–149.
- [47] L. J. Deng, T. Z. Huang, X. L. Zhao, and T. X. Jiang, "A directional global sparse model for single image rain removal," *Appl. Math. Model.*, vol. 59, pp. 662–679, 2018.
- [48] T. X. Jiang, T. Z. Huang, X. L. Zhao, L. J. Deng, and Y. Wang, "A novel tensor-based video rain streaks removal approach via utilizing discriminatively intrinsic priors," in *Proc. IEEE Conf. Comput. Vision Pattern Recognit.*, 2017, pp. 2818–2827.
- [49] X. Kuang, X. Sui, Q. Chen, and G. Gu, "Single infrared image stripe noise removal using deep convolutional networks," *IEEE Photon. J.*, vol. 9, no. 4, pp. 1–13, Aug. 2017.



Yong Chen received the B.S. degree in School of Science from East China University of Technology, Nanchang, China, in 2015. He is currently working toward the Ph.D. degree with the School of Mathematical Sciences, University of Electronic Science and Technology of China (UESTC), Chengdu, China.

His research interests include remote sensing image processing and sparse optimization.



Ting-Zhu Huang received the B.S., M.S., and Ph.D. degrees in computational mathematics from the Department of Mathematics, Xian Jiaotong University, Xian, China.

He is currently a Professor with the School of Mathematical Sciences, University of Electronic Science and Technology of China, Chengdu, China. His research interests include scientific computation and applications, numerical algorithms for image processing, numerical linear algebra, preconditioning technologies, and matrix analysis with applications.

Dr. Huang is an Editor for the *Scientific World Journal*, *Advances in Numerical Analysis*, the *Journal of Applied Mathematics*, the *Journal of Pure and Applied Mathematics: Advances in Applied Mathematics*, and the *Journal of Electronic Science and Technology*, China.



Xi-Le Zhao received the M.S. and Ph.D. degrees from the University of Electronic Science and Technology of China (UESTC), Chengdu, China, in 2009 and 2012.

He is currently a Professor with the School of Mathematical Sciences, UESTC. His research interests include the models and algorithms of high-dimensional image processing problems.